

Department of Mechanical Engineering
National Chung Hsing University
Master's Thesis

Topology Optimization for the Design of Selective
Laser Melting Support Structures to Minimize
Thermal Distortion

Advisor: Jyun-Rong Zhuang
Student: Marco Jose Zuniga Orban

April X, 2025

Abstract

This study explores the application of topology optimization in designing support structures for components manufactured using additive manufacturing, with a focus on the impact of these structures on component deformation and stress. Utilizing the SIMP method coupled with hyperbolic tangent filtering and a multivalued objective function that considers both thermal and mechanical compliance, parametric studies were conducted to investigate the effects of varying hyperbolic tangent angles, volume fractions, objective function weights, and boundary conditions. The research centered on optimizing support structures for a femoral component used in total knee arthroplasty prostheses, as well as simpler geometric shapes. The findings indicate that mechanical compliance has a negligible effect on the objective function and can be disregarded. Furthermore, the results show that hyperbolic tangent angle, boundary conditions, and volume fraction have minimal influence on average nodal displacement and stress values. Notably, the simulation of the femoral component revealed a local minimum in maximum nodal deformation within the 40% to 50% volume fraction range, suggesting that topologies with volume fractions within this range may yield more favorable outcomes, while those with lower volume fractions may result in higher maximum deformations. These insights contribute to the understanding of topology optimization in additive manufacturing, particularly for complex components like those used in prosthetic devices.

Keywords: *additive manufacturing, topology optimization, support structure design, parametric study, thermal displacement, residual stress*

Contents

1	Introduction	2
2	Literature Review	4
2.1	Introduction	4
2.2	Topology optimization	7
2.2.1	Formulation	7
2.2.2	Homogenization and SIMP	9
2.2.3	Filtering techniques	11
2.2.4	Threshold projection	13
2.2.5	Final formulation of the topology optimization problem	15
2.3	Summary of literature	17
2.4	Research purpose, originality, and contribution	18
3	Methodology	21
3.1	Introduction	21
3.2	Component CAD	21
3.3	Topology optimization model	25
3.3.1	Design domain	25
3.3.2	Objective functions	25
3.3.3	Topology optimization equations	27
3.4	COMSOL implementation	27
3.4.1	Mesh	27
3.4.2	Physical parameters	29
3.4.3	Parametric study	31

3.4.4	Boundary conditions	33
3.4.5	COMSOL implementation final details	34
3.5	Support structure design and merging with part	35
3.6	Simulation of manufacturing process	36
3.6.1	Process properties	36
3.6.2	Machine and build parameters	37
3.6.3	Convergence analysis	38
3.6.4	Voxelization and numerical parameters	40
3.7	Results and analysis	42
4	Results	43
4.1	Results of simple geometry simulations	43
4.2	Results of femoral components	53
4.2.1	Displacement analysis	53
4.2.2	Stress analysis	60
5	Discussion and conclusions	65
5.1	Conclusions	65
5.2	Future research	66

List of Figures

2.1	Smoothed modified Heaviside filters with $\eta = 0.3$, $\eta = 0.8$, and different values of β	14
2.2	Hyperbolic tangent filter function with $\eta = 0.3$, $\eta = 0.8$, and different values of β	15
3.1	Process diagram.	22
3.2	Dimensions of cube component.	23
3.3	Dimensions of triangular parts.	23
3.4	Dimensions of rounded parts.	23
3.5	Components of total knee arthroplasty prosthesis. Taken from [60]. . .	24
3.6	CAD model of femoral component.	24
3.7	Examples of design domains.	26
3.8	Mesh of the design domain for one of the rounded parts.	28
3.9	Mesh of the design domain for the support structure of the femoral component.	29
3.10	Layer heating cycle.	31
3.11	Boundary condition examples for design domain of cube component. .	33
3.12	Variation in topology due to material prescribed density at the side boundary of design domain.	34
3.13	Examples of resulting topologies from COMSOL.	34
3.14	More examples.	35
3.15	Melds of support structures for cube and rounded part.	36
3.16	Meld of supporting structure for femoral component.	37
3.17	Results of convergence test on selected parts.	41

4.1	Topology key explanation.	45
4.2	Results of cube.	46
4.3	Results of 15°triangle.	47
4.4	Results of 30°triangle.	48
4.5	Results of 45°triangle.	49
4.6	Results of 20R fillet.	50
4.7	Results of 30R fillet.	51
4.8	Results of 40R fillet.	52
4.9	Density distribution of nodal displacements, grouped by volume fraction and hyperbolic tangent angle.	54
4.10	Average nodal displacement for femoral component simulations. The left graph shows the average deformation for each topology investigated, the right graph shows the average deformation of topologies when grouped by volume fraction.	55
4.11	Maximum nodal displacements for the femoral component simulations. Notice that there are three topologies that show an excessive maximal displacement. These displacements are very likely to be outliers, and further analysis was done to understand their nature.	55
4.12	Screenshot of abnormal voxel behavior from simulation result. The voxel seems to be deformed and merging inside the structure itself. Luckily, only a handful of voxels of these sort exist, with the rest of the geometry showing much more sensible results.	56
4.13	Maximum nodal displacement after corrections.	57
4.14	Box and whisker plot for femoral displacement of all topologies.	58
4.15	Distribution of node stresses of support structures for femoral component.	61
4.16	Average node stress for supporting structure of femoral component. . .	63
4.17	Maximum node stress for supporting structure of femoral component. .	63
4.18	Box-and-whisker plot of nodal stress values of topologies of femoral com- ponent.	64

List of Tables

3.1	Physical properties of 316L steel.	30
3.2	Variation of parameters.	32
3.3	Laser parameters	38
3.4	Scanner parameters	39
3.5	Thermal parameters	39
3.6	Advanced thermal parameters	39
3.7	Parameters of support structures and geometries for convergence study.	40
4.1	Bins of nodal displacement for suspicious results. The bins labeled with an asterisk have very little to no members, indicating a discontinuous nodal deformation distribution. This is deemed to be non-physical and likely an error with the finite element result.	57
4.2	Statistics of nodal displacements (mm); all topologies	59
4.3	Statistics of nodal stresses (MPa); all topologies.	62

1. Introduction

Osteoarthritis is a very common type of arthritis that causes pain, swelling and stiffness in various body parts such as the hands, hips, back and knees. Over time, it affects bones, cartilage and other tissues, and is common in adults over the age of 45. Knee osteoarthritis, also known as degenerative joint disease of the knee, is a type of osteoarthritis that is predominantly seen in the elderly, and is a progressive disease that results in knee stiffness and swelling and pain after sitting or staying still for a long time. Although this disease can be treated, but not cured, with physical therapy and medications that slow down its progression, severe knee osteoarthritis can only be resolved by means of surgery, in which the whole knee is replaced by a prosthesis. Total knee arthroplasty (TKA), also called total knee replacement (TKR) is a very effective and consistently successful surgery that provides good outcomes for patients suffering from end-stage knee osteoarthritis. TKR results in greatly improved pain relief and better quality of life for patients [1].

Since osteoarthritis is a disease most commonly seen in the elderly, as the percentage of elderly people in developed countries around the world increases, the prevention and treatment of diseases like osteoarthritis become more important from a public health perspective. In particular, Taiwan has already exceeded the threshold (14%) of the definition of aged society established by the United Nations, with 3.983 million citizens over the age of 65, accounting for 17.18% of the population [2]. Additionally, it has been estimated that Taiwan's National Health Insurance already spends 5% of its total expenditure on TKR every year, and the incidence of TKR has already tripled in the period between 1996 and 2010 [3].

There has been a growing interest of using additive manufacturing (AM) for the creation of prosthetics used in TKA, due to it being well suited for the creation of cus-

tom, lightweight components with complex geometries, while also producing less waste compared with other methods of manufacture [4]. Even though additive manufacturing offers many advantages for the production of structures tailored to each individual patient, one of the major obstacles that stands in the way of a more widespread adoption are the high costs of AM. One way to reduce the cost of the total procedure is by reducing the amount of material used, which can also be accomplished by reducing the amount of scrap from the fabricated parts. In additive manufacturing, much of the scrap comes from discarding the support structures that the components require for manufacturing, and making smaller support components or using smaller volumes for them would be a valid strategy to reduce the cost of prosthetics. The total deformation of the part after manufacture is also an important factor to consider, since additional costs can be incurred from the addition or removal of material from the manufactured component by means of machining, in order to meet tolerances.

Topology optimization is a mature method that is able to design complicated structures based on certain governing equations and restrictions. It is also already being studied and applied to design both components and support structures manufactured through additive manufacturing. One of its strongest advantages is the ability to create optimal structures for support and heat transfer while at the same time minimizing the amount of volume and material used. This has the potential of aiding manufacturers in reducing material usage and cost while maintaining part performance. This study analyzes the process of utilizing topology optimization for the creation of support structures and simulates the deformation of a femoral component using FEM software. Additionally, it studies the impact of several topology optimization parameters on the final product, to try to determine whether an optimal set of parameters exist that might reduce the amount of material used while keeping the deformation of the component as minimal as possible.

2. Literature Review

2.1 Introduction

Additive manufacturing, also known as 3D printing, is a manufacturing process in which parts are built by stacking layers of material on top of each other until the desired geometry is created. In particular, powdered-bed fusion is a type of additive manufacturing in which the base material is composed of a metallic powdered. A bed is then filled with this powder, and a high-powered laser or electron beam is utilized to selectively add heat to locations of this powdered metal, thus melting it. As the melted portions cool, it leaves a layer of solid material, and the whole component is then built layer by layer in this manner. If a laser is used for manufacturing, the process is then known as laser powder bed fusion (LPBF).

PBF involves the layer-by-layer addition of material in which a heat source selectively melts and fuses regions of a powder bed to form a solid structure. When the material is melted and fused by using a laser, the process is called selective laser melting (SLM). The starting point of selective laser melting is a 2D computer-assisted design (CAD) model, which is sliced into 2-dimensional pieces, and later uploaded to an SLM machine. The machine then uses the laser to melt layers of powder following the information of the sliced model. At the end of each slice, the layer is left to cool down and solidify, and a new layer of powder is evenly distributed using a coater, and the melting process begins anew, until the final geometry has been reached [5]. The part is then removed from the powder bed where it might then undergo different post-processes, such as removal of supporting structures, heat treatment, or any other additional or removal of material to achieve the required dimensions and tolerances.

Additive manufacturing in general allows for the creation of parts with complex geometries that would otherwise be difficult, time-consuming or too costly to manufacture with other more traditional means of manufacturing such as machining or casting. This can be compared with the manufacture of prostheses using traditional manufacturing, which relies on the high-volume production of standardized parts and shapes. Due to the ease of creating parts with complex geometries and with shorter lead times, additive manufacturing has had a growing interest from the medical industry for the creation of custom-made implants tailored to an individual patient's anatomy [6] [4]. Additionally, this benefit of creating customized parts also leads to an improvement of patient comfort and better outcomes in orthopedic and surgical applications, as well as enhancing surgical precision and reducing complications of post-operative care [7] [8].

Despite its advantages in creating components with complex free-form 3D geometry, SLM still faces many challenges that limit its application and development. Some of these challenges are related to the development of excessive deformation, thermal stresses, and other mechanical defects such as delamination, distortion and microcracks that result from the great thermal gradients that occur within the component as it is being built, caused by the high heating and cooling rates inherent in the process [9].

Additionally, even though additive manufacturing is a viable alternative for the production of complex-shaped components, its cost can still remain high due to machine, material and process-level expenses. In particular, as a means of creating medical implants for knee-replacement therapy, the high cost of AM limits its usage for revision procedures, i.e. second or third procedures in which the objective is to replace a failed or uncomfortable component [4]. To solve the problem of high material costs, Laureijs et al. [10] have identified that one of the main driving costs is the price of the powder price. One of the viable options to drive down the price of prostheses created using additive manufacturing would be to reduce the amount of scrap material involved in the process. Scrap material in additive manufacturing results from discarding the support structures that the part requires as well as any addition or removal of material to the part in post-processing steps to ensure that the part is maintained within tolerances

[10].

The support structures alluded to in the previous paragraph refer to the structures that are built alongside the manufactured component that serve to stabilize it during the printing process. These structures are used to aid with supporting overhang areas, which are defined as areas in the structure that are almost horizontal. Support structures can also facilitate the remove of the part from the base plate and other workpieces, and can also aid with thermal diffusion or prevent residual stresses caused by thermal gradients [11].

The design of support structures in additive manufacturing is thus an important consideration, with many factors affecting how the support structure will be built. A well optimized and design support structure will enable the part to be realized, while at the same time using the least amount of material possible to obtain a specified objective. Thermal and mechanical requirements are usually at the forefront of support structure design as they have a direct effect on the quality of the component, although there might be other considerations for the design, such as ease of removability, build time, and material efficiency. Additionally, large portions of surfaces that are almost horizontal and that are unsupported during manufacturing tend to be heavily distorted after manufacturing [12]. At overhang regions, support structures are also required to be as stiff as possible to withstand the weight of the part itself and prevent it from distorting during the building process [13] [14]. Another important factor that impacts the design of support structure is the structure's performance to transfer heat away from the build component, since high thermal conduction can improve the cooling process during fabrication, which helps prevent issues caused by excessive thermal deformation such as thermal residual stresses, thermal dilation, cracks or warping [12] [15].

Topology optimization is a method that is well-suited for the creation and optimization of shapes that satisfy specific constraints while realizing certain objectives [16], and is a well-known technique that has been obtaining more interest from the additive manufacturing community for both the design of the components themselves and for their support structures in additive manufacturing. Topology optimization has

been studied for designing parts that either have as little overhang surfaces as possible, thus requiring less supporting structures, or for designing parts that are self-supporting, thus requiring no supporting structures at all. Although this aid considerably in reducing the amount of material used, these approaches do not take into consideration other effects such as the thermal dissipation of the component, or require changing the geometry of the component, thus impacting its functionality [17]. Changes in the geometry of the component might also impose geometrical constraints that can restrict the part's performance [18]. Therefore, instead of using topology optimization to change the shape of the part, much research has been made to apply topology optimization to the design of the support structure itself.

Since topology optimization is one of most popular methods for the design of support structures and the central idea used for this thesis, the following section will consist of an overview of the main ideas and implementation of topology optimization.

2.2 Topology optimization

2.2.1 Formulation

Topology optimization is an optimization technique that seeks to find the optimal shape within a volume that satisfies certain governing equations while at the same time satisfying specific constraints. This technique is usually utilized for the design of structures with no preconceived shape. Mathematically speaking, topology optimization seeks to find the optimal distribution of a design variable ρ within a design domain Ω . The placement of ρ will also obey certain governing equations that are valid within the domain, and the existence of this distribution of ρ will also depend on a certain objective that is wished to be minimized, alongside other constraints that might be imposed in the system. A classical example of topology optimization is the so called binary compliance problem, in which regions of solid and void material are distributed inside a volume, with the intention of designing a structural component that will be able to

withstand certain loads applied to its boundaries, but that will have the least amount of deformation possible. Additionally, this structure should at most use a specified fraction of its design volume, or its total weight must be kept within a certain limit. We can express this specific problem mathematically as:

$$\text{minimize } c(\boldsymbol{\rho}) = \mathbf{F}^T \mathbf{U} \quad (2.1)$$

$$\text{subject to } \mathbf{K}(\boldsymbol{\rho}) \mathbf{U} = \mathbf{F} \quad (2.2)$$

$$V = \sum_{i \in \mathbb{N}_e} \rho_i v_i \leq V_c \quad (2.3)$$

$$0 \leq \rho_{min} \leq \rho_i \leq 1, \quad \forall i \in \mathbb{N}_e \quad (2.4)$$

where in equation 2.1 the objective function that is to be minimized is given by $c(\boldsymbol{\rho}) = \mathbf{F}^T \mathbf{U}$, where ρ takes the value 0 or 1 depending on whether our small region in space is empty or contains material, \mathbf{U} is the displacement of piece of material, \mathbf{F} is the force applied to it, and \mathbb{N}_e is a finite set of elements inside the design domain Ω . The quantity c is referred to as compliance, and physically it is the inverse of the stiffness of the structure. The deformation of this material in the design domain is controlled by Hooke's Law, which is shown in equation 2.2. $\mathbf{K}(\boldsymbol{\rho})$ is defined as a global stiffness matrix [19]

$$\mathbf{K}(\boldsymbol{\rho}) = \sum_{i \in \mathbb{N}_e} \mathbf{K}_i(\rho_i) \quad (2.5)$$

where ρ_i is the density at each region i , and we assemble all those densities into the vector $\boldsymbol{\rho}$.

More generally, the formulation of topology optimization can be written as a minimization problem over a domain subject to one or more constraints, where the quantity that is being minimized is called the objective function. This objective function in turn could be an assembly of sub-objectives, each with its own relative weight with respect to the final solution. The minimized quantity is also written as a function of the

design variables, which in most topology optimization problems refers to the amount of material that is present in a small region of the design domain. Additionally, we might impose an upper limit of the total amount of volume used. This was shown in equation 2.3, where the maximum allowed volume fraction of the design domain Ω is denoted as V_c . Mathematically, the generalized problem of topology optimization can be formulated as follows:

$$\begin{aligned}
 & \text{minimize} && X_{obj} = w_1 O_1 + w_2 O_2 + \dots + w_m O_m \\
 & \text{subject to} && \text{governing equations} \\
 & && V = \sum_{i \in \mathbb{N}_e} \rho_i v_i \leq V_c \\
 & && 0 \leq \rho_{min} \leq \rho_i \leq 1, \quad \forall i \in \mathbb{N}_e \\
 & && w_1 + w_2 + \dots + w_m = 1
 \end{aligned} \tag{2.6}$$

where O_1, O_2, \dots, O_m are the sub objectives, and w_1, w_2, \dots, w_m their respective relative weights.

2.2.2 Homogenization and SIMP

Unfortunately, the formulation above suffers from a major problem. Stated as is, the problem above is well-known to be ill-posed [20], as it is possible to obtain a chattering design with an infinite number of holes of infinitesimal size, thus rendering this compliance problem to be unbounded [21]. To remedy this situation, several approaches have been proposed in the literature. One approach to control the chattering design is ensure that the total perimeter of the resulting structure has an upper bound [22] [23], but this method suffers from several complications in implementation, and small variations in the parameters of the algorithm can lead to wildly different designs of the final structure [23].

A different alternative would be the utilization of a homogenization method [24],

[25] [26] in which the binary representation of the material within the design domain is relaxed and intermediate values of densities are allowed, instead of just allowing empty and filled-values. One of the difficulties with using the homogenization method is how to interpret the intermediate densities of the material. In topology optimization problem involving the design of fluid flow media, the minimum value of the density could be interpreted as a fluid, the maximum value could be interpreted as a solid, while intermediate values could be interpreted as porous media [27]. In structural problems, intermediate values could be interpreted as periodic composite materials with high-resolution microscopic features [28] [29], materials that are composed of lattice structures [30], or even complex structures consisting of anisotropic fiber-reinforced composite materials [31]. Although the homogenization method is successful in solving the chattering design problem, validation of the resulting topologies using most Finite Element Method (FEM) software is very computationally expensive, since the resulting microstructures requires very fine meshes with high number of elements and nodes [32]. Additionally, the use of microstructures can also lead to stress amplifications which need to be managed appropriately to avoid regions of high stress concentration that might compromise the stability or functionality of the manufactured part [33]. It is also worthy of note that when this method was introduced back in the 1980's, manufacturability of components designed with the homogenization method was not feasible, as it was very difficult to manufacture components with microstructures or lattices. Nevertheless, the recent progress of additive manufacturing has revived the interest for structures with microstructures due to their newfound manufacturability [34].

A simpler method that tries to avoid the complications of homogenization theory is the Solid Isotropic Material Penalization method (SIMP), which utilizes yet another continuous density function. The main point of SIMP is to apply a power-law interpolation function to the material density, with the objective to penalize intermediate densities and drive them to their extreme values of void and full material. [35] [36]. This method was beneficial at the time this method was being developed in the late 80's and 90's, since as previously mentioned, it was yet fairly difficult to manufacture parts

with complicated microstructures, and thus methods that drove densities to a binary result of void and material were preferred. Additionally, since the implementation of this method is simpler and less computationally intensive than homogenization, many modern FEM software use SIMP for topology optimization [37].

To understand its implementation, let us return to the problem of the design of a support structure by minimizing its compliance (equations 2.1 - 2.4). Since the material density is allowed to take intermediate values, the same applies for the structure's mechanical properties, and therefore Young's modules could be computed using the following power law:

$$E_i = E_i(\rho_i) = \rho_i^p E_i, \quad (2.7)$$

where E_i is the modulus of elasticity at a region i of the design domain Ω , ρ_i is the density field at that region i , E_0 is the modulus of elasticity of the solid material and p is the penalization factor that tries to drive the density towards its binary void and solid values. However, since the SIMP method is usually used in conjunction with FEM to solve for the density distribution, it is required to avoid void material configurations that would result in singularities during the numerical computation steps. Instead, we can rewrite equation 2.7 as:

$$E_i = E_i(\rho_i) = E_{min} + \rho_i^p (E_0 - E_{min}), \quad (2.8)$$

in which the addition of the E_{min} avoids singularities, and E_0 can be chosen to be small to represent regions of void material.

2.2.3 Filtering techniques

Unfortunately, usage of the SIMP method as stated in 2.8 can also result in checkerboard patterns or might add very thin details that are comparable in size to the mesh size, causing the final result to converge to a very different topology depending on the of the

length scale of the mesh [38]. One of the possible techniques in the literature used to solve this problem is the use of filtering techniques on the density field. The main idea of these filtering techniques is to modify the density field at a point so that it becomes a weighted average of the densities of its neighboring points. Using this idea, a new filtered density field can be mathematically defined using the following equation [21]:

$$\bar{\rho}_i = \frac{\sum_{j \in N_i} H_{ij} v_j \rho_j}{\sum_{j \in N_i} H_{ij} v_j}, \quad (2.9)$$

where ρ_j is the density field at a small region j of the design domain Ω , v_j is the total volume of the region in consideration, and N_i is a neighboring region around v_j . The term H_{ij} is the weighing function, and it is analogous to a kernel, or convolution matrix, that is used in image processing applications to modify the properties of a pixel based on its surroundings, and that is typically used to blur, sharpen, emboss or perform other transformations to the image used (i.e. an image filtering function). H_{ij} could be defined as a function of the distance between the element and neighboring elements, and should be chosen so that it is linearly or exponentially decaying away from the element. A possible weighting function could be calculated as

$$H_{ij} = \max\left(1 - \frac{(x_j - x_i)^2 + (y_j - y_i)^2}{r^2}, 0\right), \quad (2.10)$$

where in this example, the design domain is two-dimensional, and x_i and y_i is the point in consideration, and r is the radius of filtration. In other literature, equation 2.10 is also expressed as [21]

$$H_{ij} = r - dist(i, j), \quad (2.11)$$

Where $dist(i, j)$ contains all the neighboring points j within a distance r of point i .

Another alternative to using equation 2.15 is to instead define the filter implicitly using a solution to the Helmholtz partial differential equation (PDE) using homogeneous Neumann boundary conditions that are imposed on the boundary of the design domain

[39]

$$\begin{aligned} -r^2 \nabla^2 \bar{\rho} + \bar{\rho} &= \rho \\ \frac{\partial \bar{\rho}}{\partial \mathbf{n}} &= 0, \end{aligned} \tag{2.12}$$

where r is the filter radius. The solution of this equation is a function that decays monotonically as is desired, and also preserves the volume of the design domain after the filtering process is completed. Additionally, equation 2.12 can be solved within the same finite element solver that is utilized for the solution of the whole topological optimization problem, and it requires no extra information beyond the mesh connectivity around each volume or mesh element [40]. It is also important to note that when the Helmholtz filter or any other filtering function is implemented into a finite element solver, the filter radius r must be bigger than the mesh edge size in order to obtain mesh independent results [41].

2.2.4 Threshold projection

Even though filtering is effective at solving the checkerboard design pathology, the structure that is designed can also suffer from intermediate density values. To try and converge these intermediate values into a void/solid configuration, projection functions can be used to map the results of the filtered density field into 0/1. One method proposed by Xu et al. [42] is a volume-preserving, modified continuous Heaviside function which takes the following form

$$\tilde{\rho} = \begin{cases} \eta[e^{-\beta(1-\bar{\rho}/\eta)} - (1 - \bar{\rho}/\eta)e^{-\beta}] & 0 \leq \bar{\rho} \leq \eta \\ (1 - \eta)[1 - e^{-\beta(\bar{\rho}-\eta)/(1-\eta)}] & \eta \leq \bar{\rho} \leq 1. \\ + (\bar{\rho} - \eta)e^{-\beta}/(1 - \eta) + \eta \end{cases} \tag{2.13}$$

In equation 2.13 $\tilde{\rho}$ is the new projected density value, $\bar{\rho}$ is the density value obtained

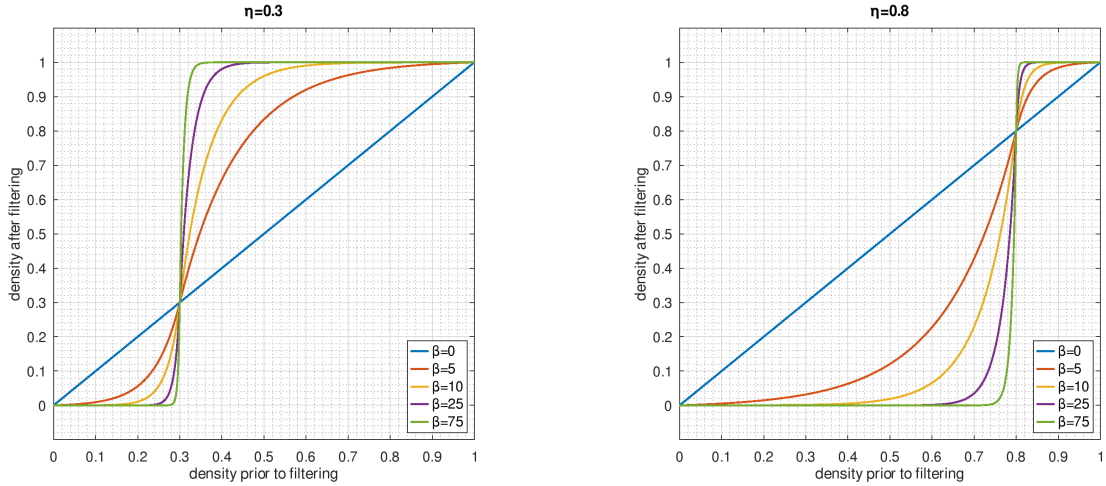


Figure 2.1: Smoothed modified Heaviside filters with $\eta = 0.3$, $\eta = 0.8$, and different values of β .

from the Helmholtz filter function explained in the previous section, η is a parameter that will determine where the cutoff point between the 0/1 values will be made in the x-axis, and β will determine how fast the transition from 0/1 will be. Figure 2.1 has been included to aid the reader in understanding how the parameters affect the shape of the function.

Although the expression in equation 2.13 is successful in projecting the filtered density values, it can be replaced by a simpler and shorter expression utilizing the hyperbolic tangent function [38]

$$\tilde{\rho}_i = \frac{\tanh(\beta\eta) + \tanh(\beta(\bar{\rho}_i - \eta))}{\tanh(\beta\eta) + \tanh(\beta(1 - \eta))} \quad (2.14)$$

Equation 2.14 has the added benefit of computing the 0/1 projection faster, and in the limit as $\beta \rightarrow \infty$ it yields the same result as equation 2.13. Plots of this equation are shown in figure 2.2.

One final point must be made before finishing this section. When a density filter is applied, the mechanical properties of the structure, such as Young's modulus or thermal conductivity, also become a function of the filtered function. For example, in the context of the structural problem described by equations 2.1 - 2.4, Young's modulus

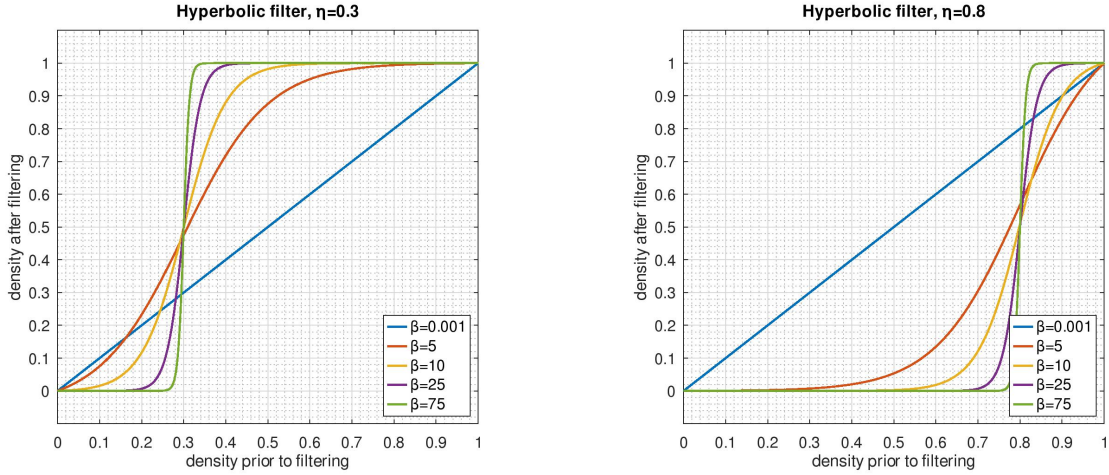


Figure 2.2: Hyperbolic tangent filter function with $\eta = 0.3$, $\eta = 0.8$, and different values of β .

described by equation 2.8 changes into the following:

$$E_i = E_i(\tilde{\rho}_i) = E_{min} + \tilde{\rho}_i^p(E_0 - E_{min}), \quad (2.15)$$

where $\tilde{\rho}_i$ denotes the filtered density using the hyperbolic tangent filter at a small element i of the design domain Ω .

2.2.5 Final formulation of the topology optimization problem

In this work, topology optimization was utilized to design a support structure for components created by additive manufacturing. The design variables are the densities of the support structure throughout its design domain, which is the volume between the component and the base plate. The objective function utilized was a multi-objective function that sought to simultaneously maximize heat conduction and minimize the compliance of the supporting structure. The material properties of the support structure that depend on the design variables are the thermal conductivity and Young's modulus. A Helmholtz filter was utilized, and the final density was computed using a hyperbolic tangent projection. Additionally, a volume fraction constrain was employed with the intention of reducing the amount of material used. Mathematically, all of

these conditions can be represented as follows:

$$\text{minimize} \quad X_{obj} = w_1 \mathbf{F}^T \mathbf{U} + w_2 \mathbf{Q}^T \mathbf{T} \quad (2.16)$$

$$\text{subject to} \quad \boldsymbol{\kappa}(\tilde{\boldsymbol{\rho}}) \mathbf{T} = \mathbf{Q} \quad (2.17)$$

$$\mathbf{K}(\tilde{\boldsymbol{\rho}}) \mathbf{U} = \mathbf{F} \quad (2.18)$$

$$V = \sum_{i \in \mathbb{N}_e} \tilde{\rho}_i v_i \leq V_c \quad (2.19)$$

$$0 \leq \rho_{min} \leq \tilde{\rho}_i \leq 1, \quad \forall i \in \mathbb{N}_e \quad (2.20)$$

$$w_1 + w_2 = 1, \quad (2.21)$$

where $\tilde{\boldsymbol{\rho}} = [\tilde{\rho}_1, \tilde{\rho}_2, \dots, \tilde{\rho}_n]^T$ and the physical densities $\tilde{\rho}_i$ are defined by equation 2.14, \mathbf{U} denotes the nodal displacement vector, \mathbf{T} denotes the nodal temperature vector, \mathbf{F} is the vector of nodal forces, and \mathbf{Q} is the thermal load vector. Equation 2.16 is the objective function, with the first term being mechanical compliance, and the second term being thermal compliance, which is the inverse of thermal conductivity. Equation 2.19 is the volume constraint equation. Equation 2.17 governs the thermal conduction of the material, with the thermal conductivity matrix $\boldsymbol{\kappa}$ calculated as:

$$\boldsymbol{\kappa}(\tilde{\boldsymbol{\rho}}) = \sum_{i \in \mathbb{N}_e} [k_{min} + \tilde{\rho}_i^p (k_0 - k_{min})] \mathbf{k}_i^0 \quad (2.22)$$

where k_{min} and k_0 are the element's minimum and maximum thermal conductivities, and \mathbf{k}_i^0 is the element's conductivity matrix. On the other hand, equation 2.18 governs the deformation of the structure, with the stiffness matrix \mathbf{K} calculated as

$$\mathbf{K}(\tilde{\boldsymbol{\rho}}) = \sum_{i \in \mathbb{N}_e} [E_{min} + \tilde{\rho}_i^p (E_0 - E_{min})] \mathbf{K}_i^0 \quad (2.23)$$

with E_{min} and E_0 denoting the limits of Young's modulus, and \mathbf{K}_i^0 is the element's stiffness matrix as defined in [21].

Additionally, the reader must note that in equations 2.22 and 2.23, \sum does not

denote summation, but instead the finite element assembly operator [19].

2.3 Summary of literature

Foundational works on the theory behind topology optimization include the work of Sigmund, Bendsoe, Lazarov, Wang and others [43], [35], [24], [44], [16], [28], [39], [38], [25], [34]. All of the previous works explain thoroughly the logic, method, and implementation of topology optimization, most of them focusing on its application for structural design problems.

Topology optimization has been identified as a powerful tool for the creation of parts made by additive manufacturing and SLM. Much focus has been given to the study of distortion of AM components. Miki and Yamada [45] proposed a method utilizing topology optimization that accounts for the distortion of the manufactured part. Misiun et al. [46] studied recoater collision and global distortion of products created by AM in the context of SIMP method based topology optimization, applied to the construction of a bracket. Komini et al. [47] investigate the creation of robust topology optimization algorithms in the distortion of parts under uncertain and variable additive manufacturing processes.

There are also several papers that investigate the design of parts that do not require any support structures, instead using topology optimization to design self-supporting components. Xu et al. [48] utilized a topology optimization framework based on Moving Morphable Components and Moving Morphable Voids, while Zheng et al. [49] used implicit B-spline representations instead of voxel-shaped representations to expedite the optimisation process significantly. Other methods include placing restriction on overhang angles and orientation to avoid horizontal structures, such as the study by Weihong and Lu [50]. Although this type of method is obviously beneficial for saving efforts in post-processing and reducing material costs, some manufacturers would be unwilling to change their current designs as it would impact the functionality or requirements of their components. For example, Ameen et al. [51] studied the limitations

of self-supporting structures in additive manufacturing; parts with convex overhanging structures built without supporting structures result in considerable deformation at these locations. Shuzhi et al. [52] formulated a topology optimization method for support structures that uses the inherent strain method to constrain distortion. Lee and Xie [53] developed an optimization algorithm that detects the best locations for supports in the boundaries of the design space, which can lead to an increase in stiffness and aid in minimizing deformation.

These distortions are usually caused by high thermal gradients that create residual stresses near the molten pool. The component or the support structure could be designed to maximize its thermal conduction and lead away heat as to minimize thermal deformation. Lohan et al. [54] discuss the possible practical objectives for heat conduction topology optimization. Lohan et al. or example, [55] also studies the use of generative design algorithms to create dendritic structures that will conduct heat away from the main component. Support structures could help to dissipate heat away from the component to reduce these residual stresses. The study by Iga et al. [56] considers not only thermal loading and conduction, but also tries to incorporate convection in the topology optimization algorithm. Huang et al. [57] uses lattice support structures to maximize heat conduction but also keeping the total space of the support structure low. Miki et al. [45] and Ogawa et al. [58] incorporate transient analyses to design a support structure with maximal heat conduction. Chung [11] also explores the effect of different lattice support structure geometries on the heat conduction performance of support structures.

2.4 Research purpose, originality, and contribution

The aforementioned studies are characterized by a high degree of academic rigor; however, from the perspective of a manufacturer, the existing software solutions already incorporate proprietary algorithms tailored to their specific needs. One of the primary concern for manufacturers lies in the optimization of material usage. Consequently,

it is imperative to investigate how the parameters governing the optimization process influence the characteristics of the final product. Additionally, an exploration of the extent to which the volume fraction can be manipulated without compromising product integrity is essential. Therein lies the central focus of the present research.

Therefore, the purpose of this research is twofold: firstly, to investigate a full procedure for the design and validation of supporting structures of components manufactured through SLM utilizing topology optimization, identifying any tricky parts of the process. As mentioned before, Most studies only concern themselves on the study of topological optimization algorithms for the design of support structures, but don't delve into the full process of CAD creation and validation of the impact of the support structure on the final part by means of simulations and experiments. This work takes a look at the whole process, and discusses the challenges and opportunities for improvement of CAD creation and FEM simulation of support structures.

The second objective of this research is to investigate the influence of topology optimization parameters on the total deformation of components manufactured through Selective Laser Melting (SLM). To achieve this, various topologies for support structures were generated by manipulating parameters such as volume fraction, objective function weights, and hyperbolic tangent projection filter settings. Subsequently, simulations of the SLM component building process utilizing these structures were conducted, enabling an analysis of how different topology optimization parameters affect the total deformation and resultant stress of the finished SLM products. Particular emphasis was placed on the effect of volume fraction, with the aim of determining whether a reduction in the volume fraction of the supporting structure would adversely impact the quality of the final component.

Successfully identifying a set of parameters that yield optimal results in terms of minimizing deformation and stress can provide manufacturers with valuable insights for enhancing their manufacturing processes. Conversely, if the parameters are found to have minimal influence on the final product's quality, manufacturers may choose to adopt parameters that align more closely with their operational requirements without

the concern of compromising part integrity. For instance, if adjustments to the volume fraction of the support structure do not significantly affect the quality of the final component, manufacturers could utilize a lower volume fraction to reduce material costs while maintaining confidence in the quality of the produced parts.

Therefore, the contributions of this study to the field are as follows:

1. Investigate the impact of topology optimization parameters on the thermal deformation and stress experienced by support structures. This investigation will specifically focus on the effects of hyperbolic tangent projection, volume fraction, and the weight ratio of objective functions.
2. Identify the optimal combination of topology optimization parameters that minimizes thermal deformation and thermal stress in components produced via SLM.
3. Identify specific geometric configurations that enhance thermal deformation or stress performance, or determine configurations that maintain deformation or stress within acceptable limits while simultaneously reducing material usage.

3. Methodology

3.1 Introduction

To evaluate the performance of various support structures developed through topology optimization, a comparative study was conducted in which components fabricated via additive manufacturing were paired with distinct support structures. This investigation assumed that different structural configurations would exhibit varying thermal conductivity, thereby influencing the efficiency of heat dissipation from each material layer during the manufacturing process. Enhanced thermal conduction is anticipated to mitigate overall thermal deformation, as the manufactured component would experience reduced expansion due to a shorter duration of exposure to elevated temperatures.

This section will explain the full process employed to run the simulations and analyze the resultant data. An overview of the procedural framework is illustrated in Figure 1.1. The process starts from the creation of the CAD for the manufactured components, followed by the design and CAD creation of the corresponding support structures. The components and the support structures are then merged, and imported into the additive manufacturing software to simulate the results of manufacture. The results obtained from the manufacturing simulation are then subjected to analysis through graphical representations and statistical methods.

The subsequent sections explain in detail each stage of this process.

3.2 Component CAD

The components with simple geometries utilized in this study consist of a cube, three triangular components with different slopes, and three cylindrical components with

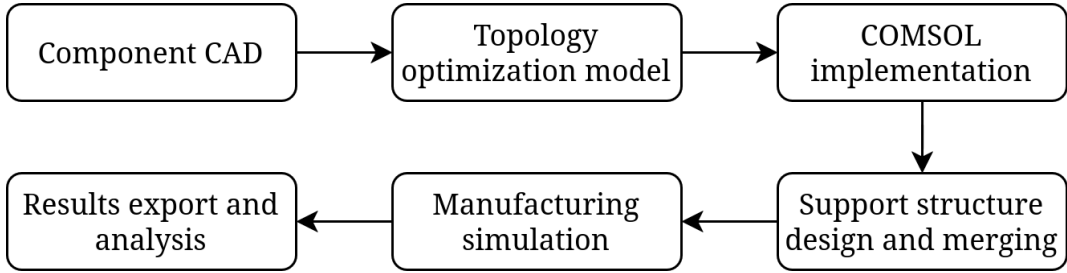


Figure 3.1: Process diagram.

different values of curvature. These shapes with these dimensions were chosen to ease the comparison of results between this study and the study of Peishu [11]. All the CAD models used for the simple geometry study were created using FreeCAD [59], an open-source CAD software. The components were exported as .stp files, and then were merged with their corresponding support structures using the software nTop. The geometries used for this preliminary study are the following:

- A cube with side length of 30 mm, as shown in Figure 1.2.
- Three triangular components with varying slopes. All triangular components have a base of $30 \times 30 \text{ mm}^2$, with slopes of 15° , 30° and 45° . The measurements are shown in Figures 1.3a, 1.3b, and 1.3c.
- Three prisms with fillets of different. The radii used were 20 mm, 30 mm, and 40 mm. These rounded prisms also have a base of $30 \times 30 \text{ cm}^2$. They are shown in Figures 1.4a, 1.4b, and 1.4c.

Apart from the parts above, a CAD model for a femoral component was also employed. The femoral component is one of the prosthetic components used in total knee arthroplasty, and is the piece that is directly connected to the patient's femur. This is shown in Figures 1.5 and 1.6.

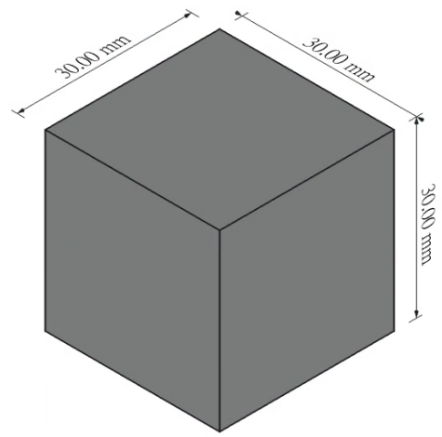
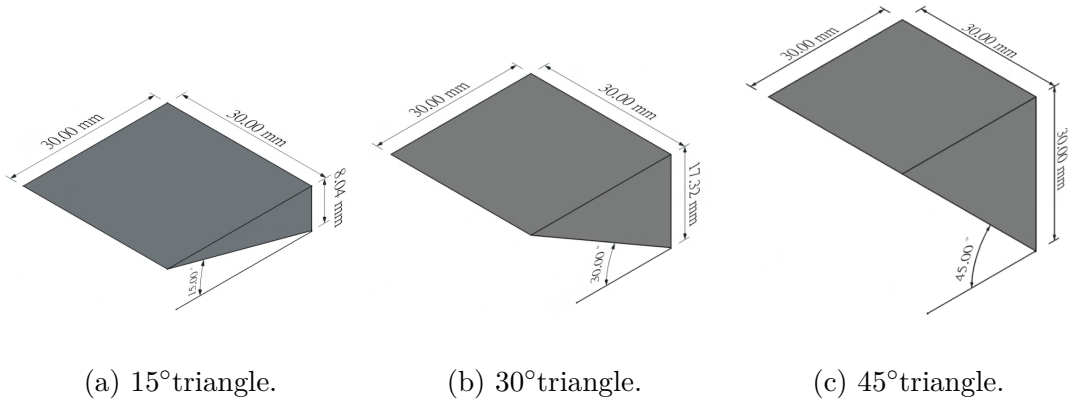


Figure 3.2: Dimensions of cube component.

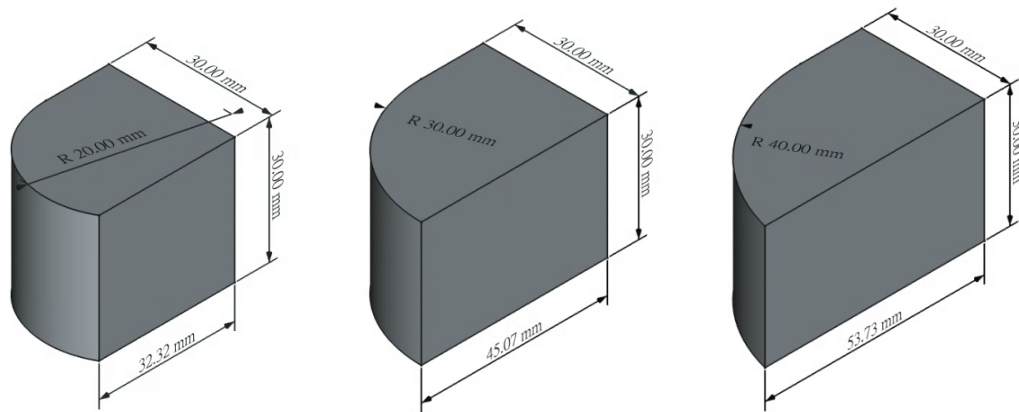


(a) 15° triangle.

(b) 30° triangle.

(c) 45° triangle.

Figure 3.3: Dimensions of triangular parts.



(a) Part with R20 mm fillet. (b) Part with R30 mm fillet. (c) Part with R40 mm fillet.

Figure 3.4: Dimensions of rounded parts.

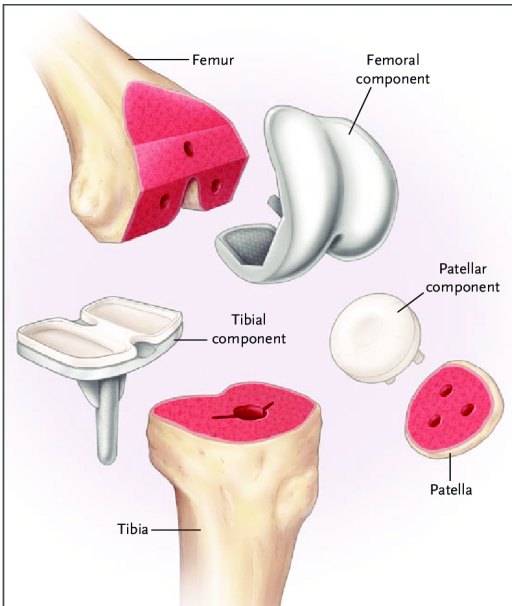


Figure 3.5: Components of total knee arthroplasty prosthesis. Taken from [60].

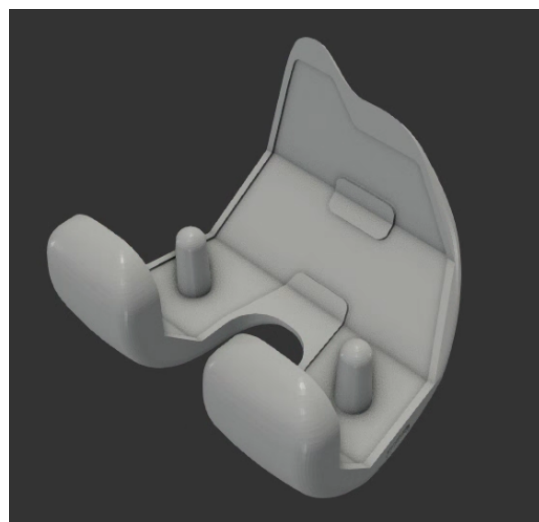


Figure 3.6: CAD model of femoral component.

3.3 Topology optimization model

The supporting structures of the components were created using the method of topology optimization. The design was implemented using the topology optimization module of COMSOL Multiphysics 6.2.

The steps for creating a valid topology optimization model are: determine the design volume, design the support structure using topology optimization, merge the support structure with the part, and carry out the FEM simulation for manufacture.

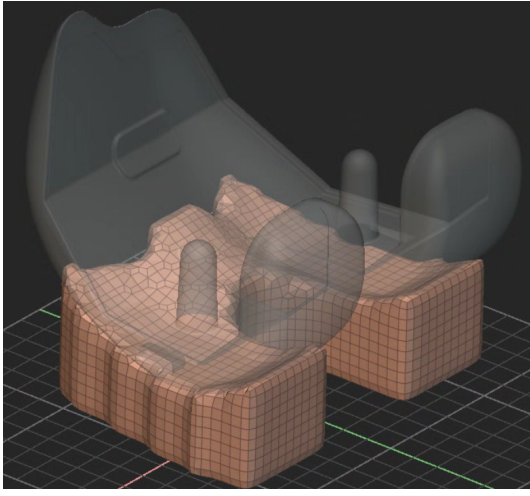
3.3.1 Design domain

The design domain consisted of the volume between the bottom face of each component and the xy plane, when the component is placed at a height of 30mm above the xy plane. For the simple geometry parts, as they have high symmetry, the design domain was just taken to be a 2D slice of the volume. The topology optimization problem was then solved for this volume, and the resulting topologies were extruded in the direction perpendicular to the design plane to cover the space underneath the part. For the femoral component, the topology optimization was directly solved in the 3D volume between the lower surface of the femoral component and the xy plane. Figures 1.7a and 1.7b show examples of design domains.

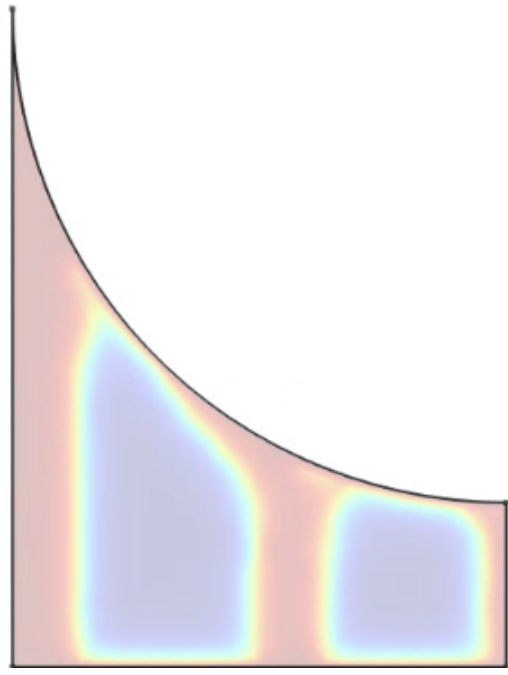
3.3.2 Objective functions

The objective of the problem is to maximize the thermal conduction of the support structure, while at the same time maximizing its stiffness. The thermal conductivity has been chosen as an objective since it is required to drive heat away from the part as fast as possible to reduce its thermal deformation. Thermal conduction is given by Fourier's law as:

$$\mathbf{Q} = -\kappa \nabla T \quad (3.1)$$



(a) Design domain for femoral component.



(b) Design domain for rounded part.

Figure 3.7: Examples of design domains.

where \mathbf{Q} is the heat conduction through the material, κ is the material's thermal conductivity and ∇T is the thermal gradient. For use in a finite element solver, the objective function c_t and Fourier's law can be written using matrix notation as:

$$\text{minimize} \quad c_t = \mathbf{Q}^T \mathbf{T} \quad (3.2)$$

$$\kappa \mathbf{T} = \mathbf{Q}, \quad (3.3)$$

where κ is the global thermal conductivity matrix, \mathbf{T} is the temperature vector, and \mathbf{Q} is the thermal load, or heat flux, vector. Thermal compliance c_t can be thought of the thermal analogy to the stiffness of a structure. In structural problems, the objective is to maximize the stiffness, or minimize the compliance, as compliance is the inverse of stiffness. Similarly, in thermal problems, the objective is to maximize the thermal conductivity, or alternatively, minimize the thermal compliance, which can be though

of as the inverse of conductivity. Thermal compliance has extensively been used in other topology optimization problems such as [61], [62], and [63].

At the same time, stiffness of the support structure should be maximized to avoid considerable deformations that might affect the part geometry. The geometry resulting from the thermal optimization could result in thin, dendrite-like structures, which could buckle and collapse under the component's weight, causing the whole manufacturing process to fail. Assuming small deformations, we can express the displacement of the material by using Hooke's law, $\mathbf{F} = k\mathbf{U}$. For finite element analysis, the minimization of the compliance c of the structure and its mechanical behavior is obtained by minimizing the quantity $\mathbf{F}^T \mathbf{U}$, by solving for \mathbf{U} using a numerical method.

We can then combine the thermal and mechanical compliance to obtain the objective function for this topology optimization problem, with ω_1 and ω_2 the weight coefficients that encapsulate the relative importance of each objective: $\omega_1 \mathbf{Q}^T \mathbf{T} + \omega_2 \mathbf{F}^T \mathbf{U}$

3.3.3 Topology optimization equations

Having decided the governing equations and objective function for the system, the topology optimization model must be chosen. For this study, the SIMP approach with a hyperbolic tangent projection has been employed, utilizing a volume fraction restriction. Mathematically, the topology optimization problem is formulated as shown in equations 2.16 to 2.21 , where the density $\tilde{\rho}$ has been defined using the hyperbolic tangent projection function as defined in section 2.2.4.

3.4 COMSOL implementation

3.4.1 Mesh

To run the topology optimization algorithm and obtain a solution, the design domain must be divided into finite element methods for computation. For the 2D design domains of the simple geometry elements, free triangular meshes were utilized, using a

predefined mesh element size of "finer". This resulted in about 2000-3000 elements for each of the design domains, depending on the geometry of the domain. These mesh parameters were chosen to produce fast results and to obtain a general idea of how the simulation parameters affected the solution of the topology optimization problem. An example of 2D mesh can be seen in Figure 1.8.

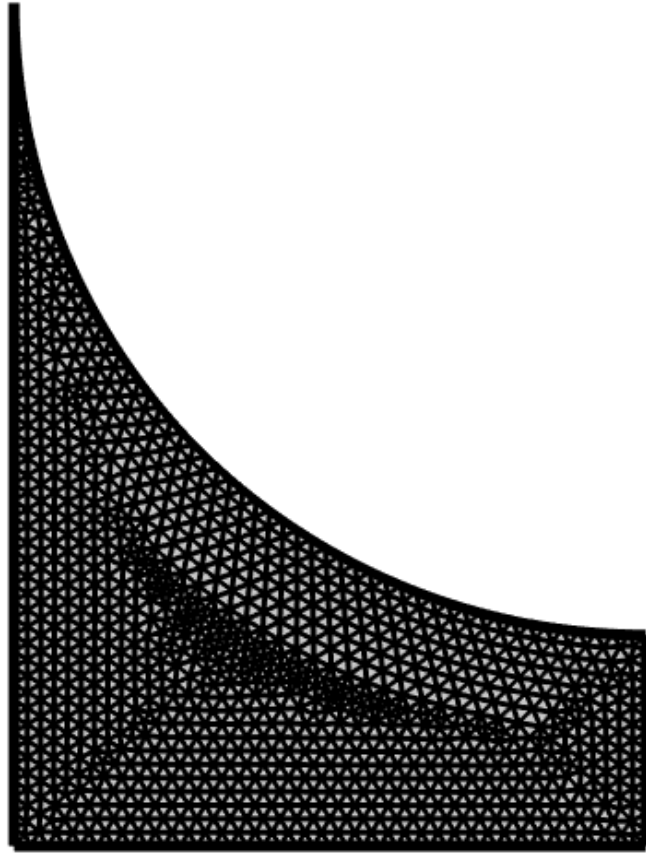


Figure 3.8: Mesh of the design domain for one of the rounded parts.

On the other hand, For the 3D design domain of the femoral component support structure, the mesh sizing parameters were chosen with more deliberation. The maximum and minimum element sizes of the mesh were determined based on the minimum element size achievable by the selective laser melting (SLM) machine utilized in this study, which is approximately 0.2 millimeters. However, employing a mesh with an element size of 0.2 millimeters results in excessively fine meshes that significantly prolong

computational solving times. Consequently, the maximum and minimum mesh sizes were adjusted to be 8 and 4 times the minimum feature size, resulting in values of approximately 1.6 millimeters and 0.8 millimeters, respectively. This resulted in meshes with approximately 164,000 elements. The resulting mesh can be seen in Figure 1.9.

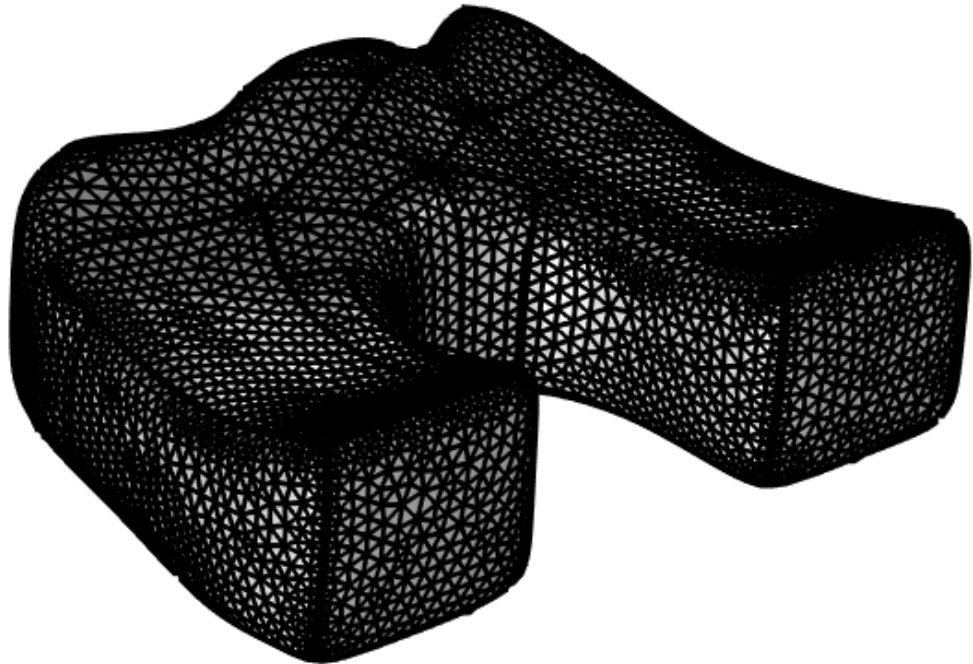


Figure 3.9: Mesh of the design domain for the support structure of the femoral component.

3.4.2 Physical parameters

For the topology optimization solution to be useful, realistic thermal and stress load should be used. The thermal load was based on the maximum wattage and efficiency of the laser achievable by the selective laser melting machine used in this work. The laser's power is 200 W, with an efficiency of 25%. This value cannot be used for the thermal

load, since the laser is only activated for a small amount of time. From the FEM software building process parameters, each layer is heated for approximately 154 ms. Therefore, with an effective power of $200 \text{ W} \times 0.25\% = 50\text{W}$, the total amount of energy added to the layer during the heating time is $50 \text{ W} \times 154 \text{ ms} = 7.7 \text{ J}$. But each layer heating time occurs periodically, with a period of approximately 440 s. Therefore, the average power input to the system per cycle is calculated to be 0.0175 W. A graphical representation of this calculation is shown in Figure 1.10. The approximate area of the top surface of the support structure design domain is approximately $30 \text{ mm} \times 30 \text{ mm} = 900 \text{ mm}^2$. Dividing the power per cycle by this area yields a heat flux of about 19.4 W/mm^2 , which was rounded up to 20.0 W/m^2 . For the heat flux used in the femoral component calculation, the difference is in the area of the top surface of the design domain. This area is about 1690 mm^2 , and thus the heat flux used for the support structure design in accounts to be about 10.37 W/m^2 , which was rounded to 10 W/m^2 .

The material used in all simulations was 316L stainless steel. This material is often used for medical implants due to its superior mechanical, fatigue, wear and corrosion properties [64]. The mechanical and thermal properties of 316L steel relevant to this study are shown in Table 1.1.

Table 3.1: Physical properties of 316L steel.

Density	8.0 g / cm ³
Thermal conductivity	15 W / (m·K)
Heat capacity	500 J / (kg·K)
Young's Modulus	200 GPa

It should be noted that the physical properties of stainless steel shown above are average properties at 20°C. These are subject to change during the building process, as the material is repeatedly heated above its melting point and cooled down, but for the purpose of simplifying the simulation process, these constant values were employed for the topology optimization problem.

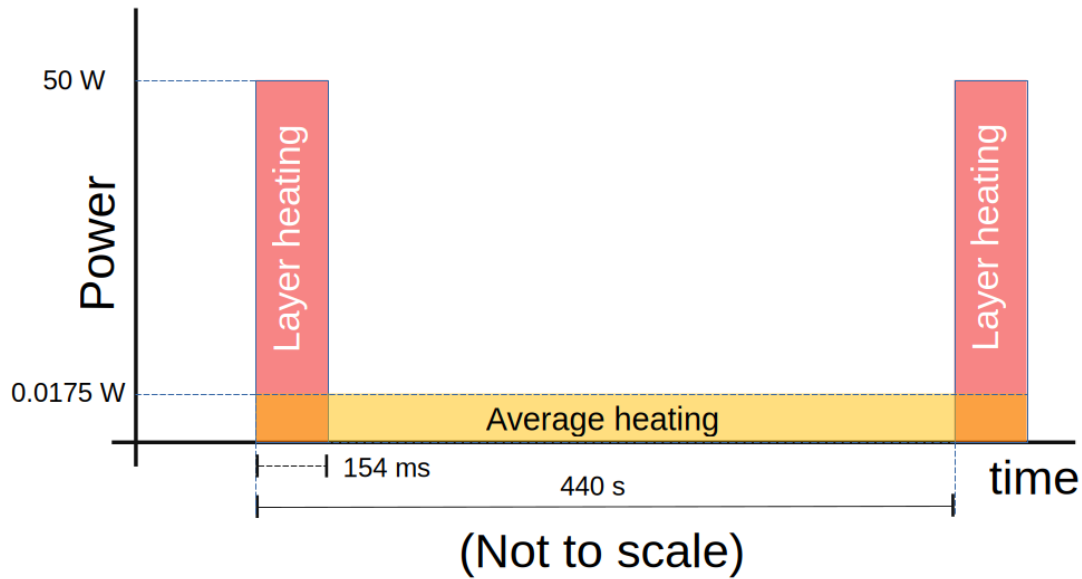


Figure 3.10: Layer heating cycle.

For the calculation of compliance, the structural load used was the stress on the top surface of the design domain caused by the weight of the component above it. This stress was calculated by diving the component's weight by the area of the top surface. The weight was determined using the density of 316L steel, which is approximately 7.93 g/cm^3 . For example, the volume of the femoral component was calculated to be about 32800 mm^3 , and therefore the mass of the femoral component amounts to approximately 0.263 kg . From this, the weight can be calculated by multiplying by the gravitational constant g , and the stress is obtained by dividing this weight by the top area of the design domain. The calculation for this example ends up being $(0.263 \text{ kg})g / 1690 \text{ mm}^2 = 1560 \text{ N/m}^2$, where g is taken to be 9.81 m/s^2 .

3.4.3 Parametric study

The topology optimization problem was solved using COMSOL Multiphysics 6.2 software. COMSOL allows the creation of parametric studies that allow to run a simulation with a list of parameters to be varied, in order to study the influence of different values on the solution of a system. For this study, the values of volume fraction 2.19, objective

Table 3.2: Variation of parameters.

Parameter	Values	
Volume fraction	Simple geometry	0.50, 0.75
	Femoral component	0.25, 0.33, 0.40, 0.50, 0.75
Hyperbolic tangent angle	Simple geometry	0.001°, 2°, 4°, 8°
	Femoral component	0.001°, 2°, 4°, 8°
Boundary conditions	All	void (no material at boundaries) material (material at boundaries)
Objective weights	Simple geometry	(0.2, 0.8), (0.5, 0.5), (0.8, 0.2)
	Femoral component	(1.0, 0.0)

function weights 2.21, and hyperbolic tangent angle (used in 2.14) were chosen as the parameters to be varied.

Volume fraction is defined as the maximum amount of volume that the topology can cover within the design domain. This criteria is chosen because we seek to use less material for the supporting structure, as long as we can maintain the total deformation of the manufacturing component beneath a threshold. For the simple geometries 50% and 75% of volume fraction were considered. For the femoral component study, volume fractions of 25%, 33%, 40%, 50% and 75% were considered.

The hyperbolic tangent angle projection (2.14) was also used as a parameter. The hyperbolic tangent was varied from a value of 0.001° to 8°, in steps in 2°. The variation was stopped at 8° since it was noticed that for $\theta \geq 8^\circ$ there would be no discernible differences between results.

Finally, the objective functions weights were also varied for the design of topologies for the simple geometry parts. The pairings of weight used were (0.2, 0.8), (0.5, 0.5), and (0.2, 0.8), where the first weight in each pair corresponds to the weight of the thermal compliance objective and the second corresponds to the weight of the mechanical compliance objective. All of these parameters are summarized in Table 1.2.

3.4.4 Boundary conditions

It is possible to change the material boundary conditions in COMSOL when solving the topology optimization problem. As an extra study parameter, the material boundary condition of several edges of the design domain were also varied for this study. For the 2D design domains, different topologies were obtained by having either a prescribed material or void boundary in the side elements of the design domain. For the femoral component, there was no variation in the density of the design domain boundary. Figures 1.12a and 1.12b shows the boundary conditions used in the problem.

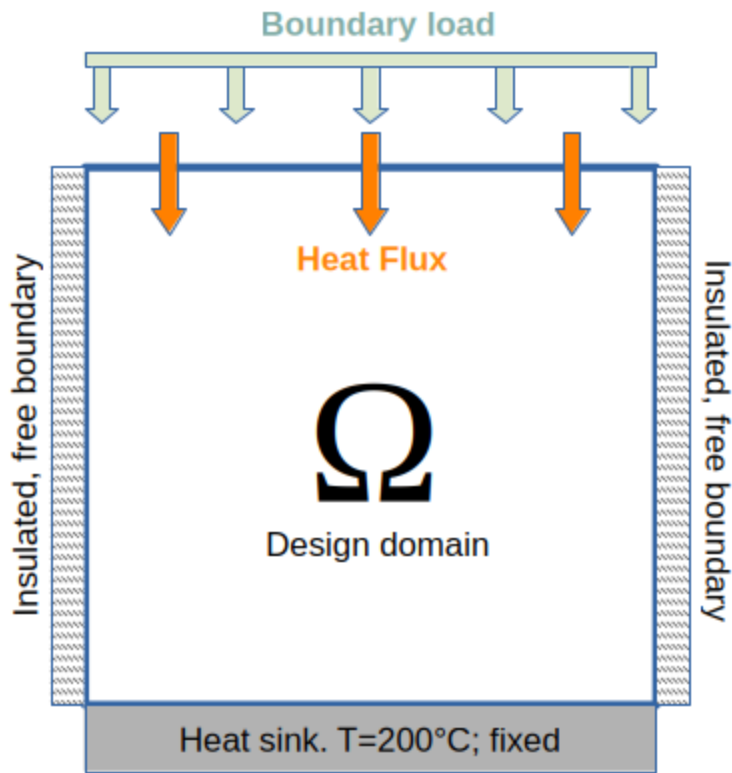
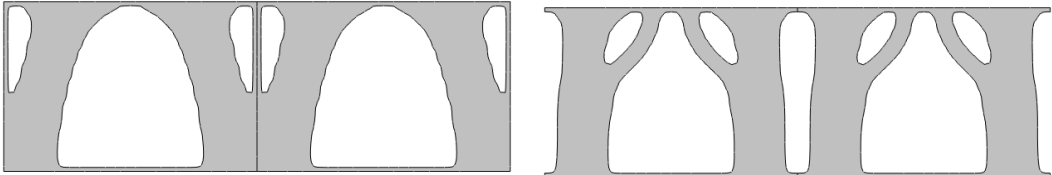


Figure 3.11: Boundary condition examples for design domain of cube component.

The heat transfer and solid mechanics boundary conditions must also be specified. The heat transfer problem boundary conditions consisted of a heat flux through the upper surface of $20 \text{ W} / (\text{m}^2 \cdot \text{K})$ and $10 \text{ W} / (\text{m}^2 \cdot \text{K})$ for the simple geometry parts and femoral component respectively. The inferior surface was set at a constant temperature



(a) Topology with solid material density. (b) Topology with void material density.

Figure 3.12: Variation in topology due to material prescribed density at the side boundary of design domain.

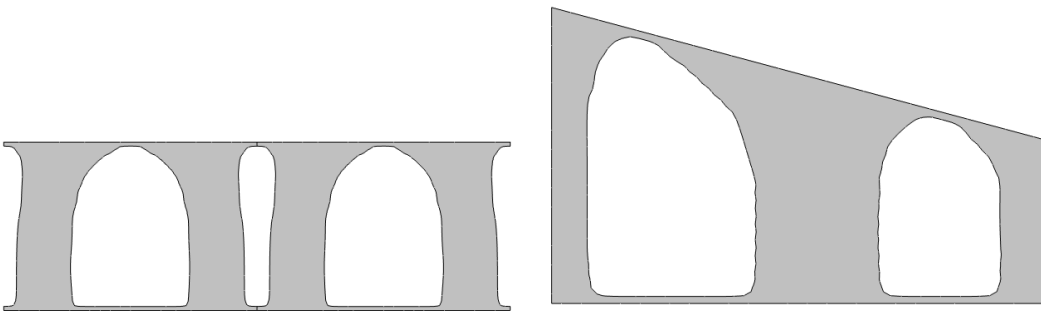


Figure 3.13: Examples of resulting topologies from COMSOL.

of 200°K , and the sides were kept insulated. The structural loads consisted of the weight of the component above it. Figure 1.11 shows a graphical representation of the boundary conditions used.

3.4.5 COMSOL implementation final details

Once all the physical and material parameters, the topology optimization model and parameters, boundary conditions, and parametric study have been set up, the solver will have all the information needed to obtain a solution. For this project, the solver algorithm utilized the method of moving asymptotes (MMA) [65], with a maximum iteration number of 50. The optimality tolerance was also set to COMSOL's default value of 0.001. Lastly, the penalty factor for the SIMP method was set to $p=3$.

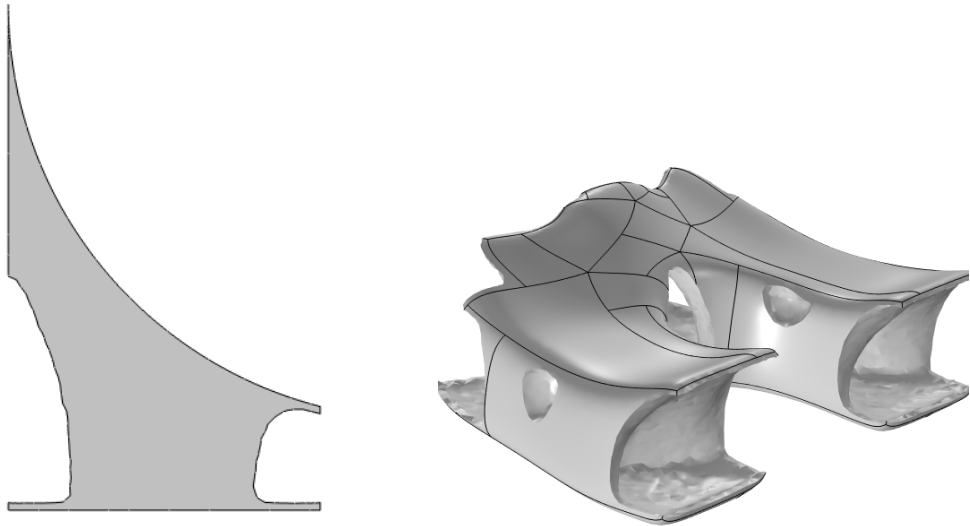


Figure 3.14: More examples.

3.5 Support structure design and merging with part

After COMSOL was used to generate the possible topologies for the support structure, the topology was exported to image files, in the case of the 2D problem, and to an .stl file, in the case of the 3D structure. These were then converted to 3D .stp file with the aid of FreeCAD. nTop Software [66] was then used to merge the resulting support structure with the manufactured components. Once the support structure and the part were joined, they were exported as .stl files to be used in the SLM finite element simulation.

Once the CAD file of the component and the support structure has been built, it is necessary to merge them together and import them into Simufact to undergo simulation of the manufacturing process. The software used for blending the component and its support structure is nTop version 5.17.2. nTop's interface makes it very easy to merge the part, and also allows to blend the support structure and the component, which effectively creates a fillet between the nodes of both components to allow for a smooth transition between bodies. Of course, blending the component and the support structure in this manner would not give any benefit in a real manufacturing process, as

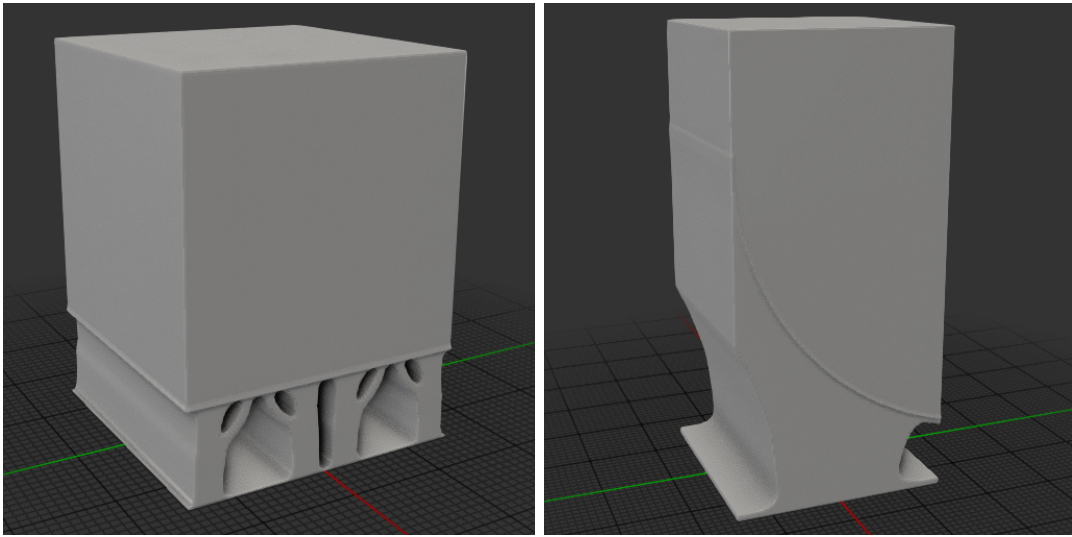


Figure 3.15: Melds of support structures for cube and rounded part.

the structure and the component would not be able to be separated easily. Nevertheless, this blend radius is beneficial for the simulation since it was observed that a direct union and import of the support structure + component in Simufact resulted in having very small gaps between the two pieces, resulting in a non manifold geometry that would cause the finite element model to have gaps between some of its nodes.

3.6 Simulation of manufacturing process

The software utilized to simulate the manufacturing process is Simufact Additive version 2023.2. Simufact Additive is capable of simulating the building process of additive manufacturing components, and coupling thermal and stress physics to predict the temperature values of the component throughout the building process and the total stresses, strains and deformations resulting from the manufacturing process.

3.6.1 Process properties

After the component and the support structures were merged, they were imported into Simufact. It is during this step that all the factors related to the simulation are set,

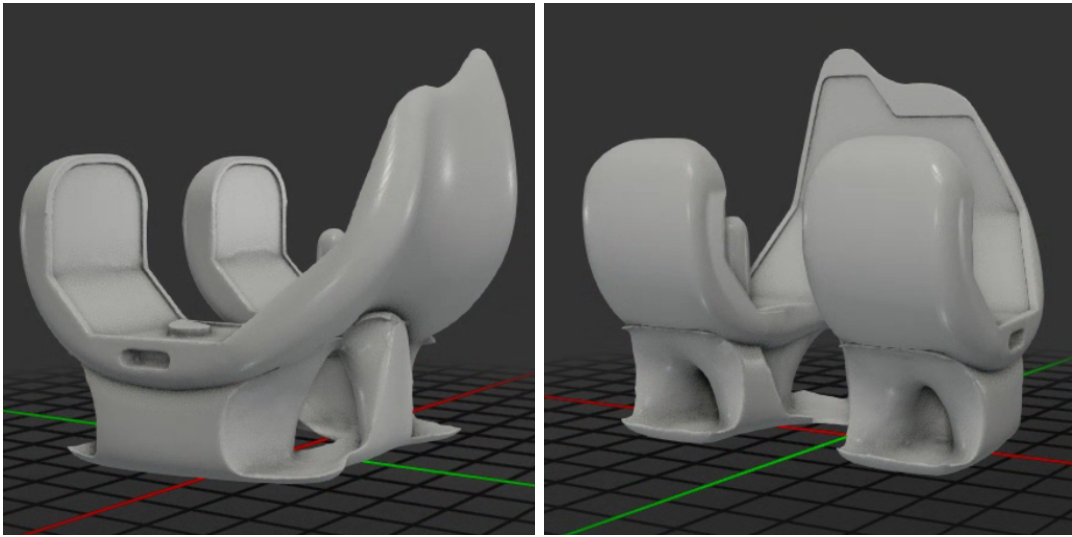


Figure 3.16: Meld of supporting structure for femoral component.

which include the machine properties, material properties, and build parameters.

The first parameter to be chosen is the process properties, which determines the physics that Simufact takes into consideration to run the simulation. Simufact provides three different types of processes: mechanical, thermal, and thermomechanical. As stated in the Simufact manual [67], mechanical provides a fast mechanical analysis that only uses inherent strains as the main input. This type of analysis does not take into consideration the temperature fields during the building process. The thermal process on the other hand only considers the thermal behaviour of the components, and the temperature field of the support structures, components and base can be analyzed. The thermomechanical process couples the stress and thermal analyses, and allows for the prediction of temperature, distortions and stresses of the part. This latter thermomechanical process is the process utilized throughout this study.

3.6.2 Machine and build parameters

After choosing the process property, the machine parameters must be specified. This includes the machine build plate geometry and the laser parameters. The machine build plate chosen was a circular plate with an 80 mm radius. The build space dimensions

Table 3.3: Laser parameters

laser power	200W
laser speed	1000 mm/s
efficiency	25%
beam width	100 μm
layer thickness	30 μm
recoater time	10 s

consists of a space of 160 mm in all three x-y-z directions. As for the laser parameters, the simulations were carried out with one laser with a maximum laser power of 500 W and a maximum laser speed of 2000 mm / s, an efficiency of 25%, and a beam width of 25 mm. These machine parameters were modeled after an AMP-160 SLM machine, manufactured by TongTai Machine & Tool Company, Taiwan, that has been used in similar studies [11], [68].

The building parameters for the process need also to be set. These include material layer parameters and any thermal parameters and temperature specifications for the build environment and base plate. The powder layer thickness was chosen to be 0.03 mm, with a recoater time of 10 s. The powder initial temperature was set to 25°C, with an initial base temperature of 200°C. Preheating is important in SLM since it can influence the quality of the microstructure of the component. It has been suggested that a temperature of 200°C exhibits higher cooling rates and smaller grain sizes of the microstructure [69].

All of the above parameters plus more are summarized in Tables 1.3, 1.4, 1.5, and 1.6.

3.6.3 Convergence analysis

To ensure that FEM results were not dependent on the voxel size of the voxel mesh, a convergence analysis was first performed on one of the simple geometries. For this

Table 3.4: Scanner parameters

scan width	20 mm
scan overlap	0 mm
hatch distance	0.07 mm
pause time	0 s

Table 3.5: Thermal parameters

powder temperature	25°C
chamber temperature	50°C
base plate temperature	200°C

Table 3.6: Advanced thermal parameters

Part / Support emissivity	0.85
Part / Support heat transfer coefficient	12.0 W/(m ² ·K)
Base plate emissivity	0.6
Base plate heat transfer coefficient	20 W/(m ² ·K)
Base plate contact heat transfer coefficient	100 W/(m ² ·K)

analysis, the results of three projects were compared. The details of the projects are shown in Table 1.7. The convergence test proved highly successful, as there is very little difference in the results of the FEM simulations between the different voxel sizes of each project. The results of the convergence test are shown in Figure 1.17. The graphs shows the average and max node deformation of the part's surface, as the voxel size is varied from 1 mm to 0.5 mm. We can see that the variability of surface results due to the voxel size is at most 0.01 mm. In subsequent analyses, the difference between average node displacements of parts with different support structures would be of an order of magnitude bigger (> 0.1 mm), and thus we can discard the possibility that differences in results are caused or are dependent on the voxel mesh size.

Table 3.7: Parameters of support structures and geometries for convergence study.

Part	Volfrac	$\tanh(\theta)$	Objective weights	Side density
Cube 1	50%	0°	w1=w2=0.5	Solid
Cube 2	75%	4°	w1=w2=0.5	Void
Triangle 15°	50%	0°	w1=w2=0.5	Solid

3.6.4 Voxelization and numerical parameters

All of the simulations run on Simufact used voxel meshes with sizes ranging from 0.8 mm to 1.5 mm, depending on the complexity of the geometry of the part. The voxelization of the components was performed with Simufact's default voxelization engine. The voxel meshes of the components were uniform in size, while the base plate voxel mesh used adaptive meshing, with 2 levels of coarsening. The solver used for all simulations was the Multifrontal Massively Parallel Sparse (MUMPS for short) Direct Solver, with 14 time steps for each voxel layer.

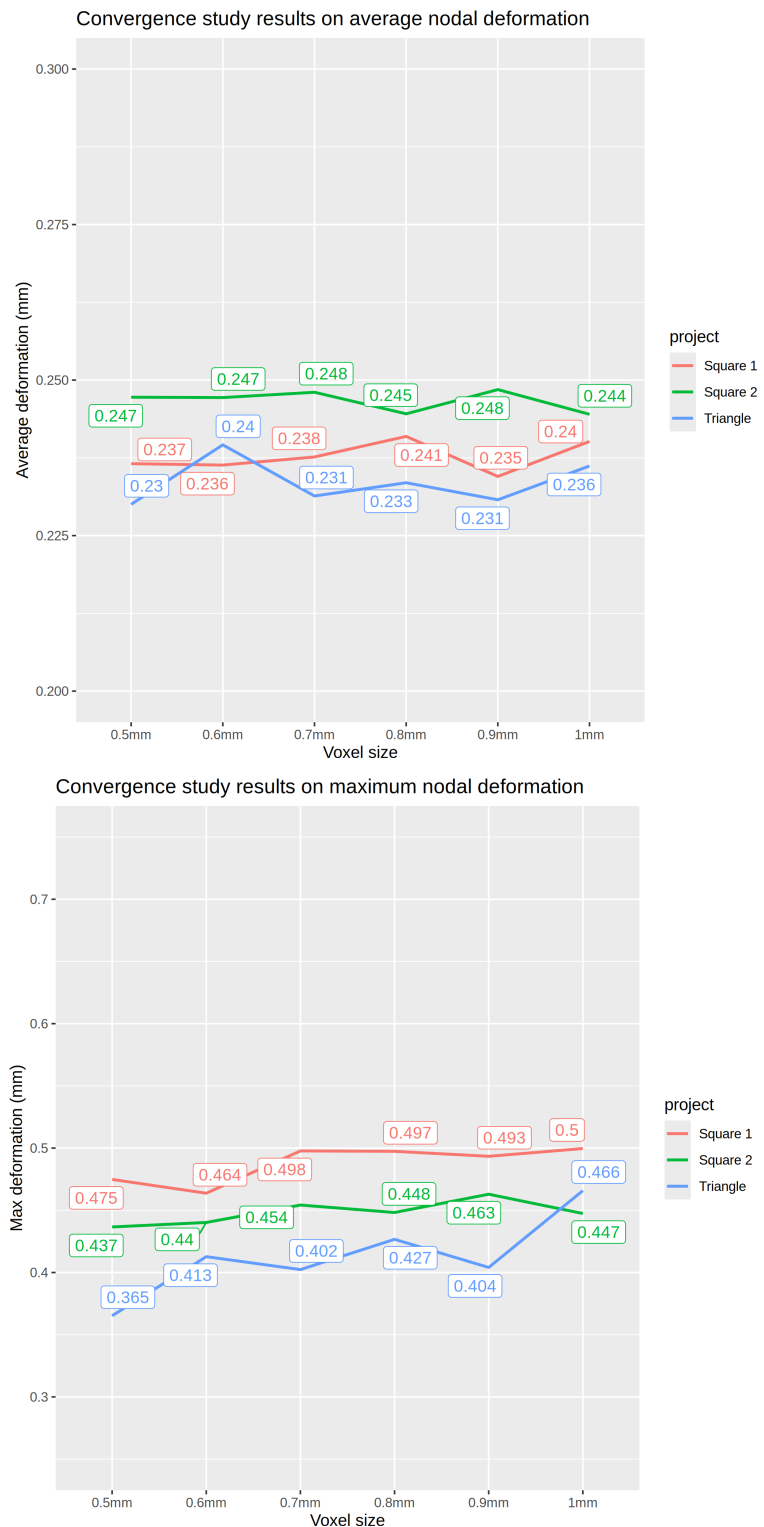


Figure 3.17: Results of convergence test on selected parts.

3.7 Results and analysis

After the simulation was run, the node displacement and stress data of last time increment was exported to a .csv file using a Python script. The .csv file was then read and parsed using R, and the data was used to obtain statistical values and graphs. The results are summarized in the next chapter.

4. Results

After the simulation ended, the displacement and stress results of the surface and volume meshes were exported as a .csv file. The surface mesh was utilized to gather statistics on the displacement of the part, to understand its overall deformation. The volume mesh was used to analyze the stress distribution within the component. R consisted of the node displacement and stress values. This information was then analyzed using R, and various plots were created using the ggplot library.

The values that are most important for this study are the average values and the maximum values, as both of these could be taken to be different criteria to compare performances. Obviously, a part with lower average displacement or lower stress will be more desirable, but it is also important to consider maximum displacement and maximum stress as well, as a part with lower average displacement but with a few nodes with very high displacement could still be considered a failed component, as it is the portions with highest deformation that will need to be processed with additional machining, or cause high discomfort in patients. Additionally, regions of maximum stress should be considered because the stress at this regions might be greater than the ultimate stress of the material, causing the component to break and fail.

4.1 Results of simple geometry simulations

This section shows the results for the simple geometry simulations, composed of a cube, three triangles with different angles, and three cubes with fillets, as explained in Chapter 1.2.

The results of the analysis indicate that there is no apparent relationship between the hyperbolic angle or boundary conditions and the observed node displacements. The

average node displacements for each topology and each project appear to be relatively stable, with no stark differences observed between the various topologies. The differences in node displacements between the topologies fall well within the uncertainty bounds of the convergence results, suggesting that the choice of topology does not have a significant impact on the overall structural behavior. These findings imply that the design parameters under investigation, such as the hyperbolic angle and boundary conditions, do not play a dominant role in driving the global structural response, at least within the range of values considered in this study.

In addition to the node displacements, the analysis also examined the average node stress and maximum node stress for each topology and project. These stress metrics were found to follow a similar trend as the average node displacements, exhibiting relatively stable values across the different topologies with no clear relationship between topology and stress levels. The differences in both average and maximum node stresses between the various topologies fall within the uncertainty bounds of the convergence results, suggesting that the choice of topology does not have a significant impact on the overall stress state of the structure. This further reinforces the conclusion that the design parameters investigated, such as the hyperbolic angle and boundary conditions, do not play a dominant role in driving the global structural response in terms of both displacements and stresses. The consistent stress and displacement behavior across topologies indicates a level of robustness in the structural performance that may be advantageous for design applications where flexibility and insensitivity to specific design choices are desirable.

While the overall trends indicate a general stability in the average node displacements and stresses across the different topologies, the analysis also revealed some notable exceptions. Specifically, certain topologies were found to result in significantly higher maximum node displacements that could not be attributed solely to the uncertainty of the convergence results. This behavior was most pronounced in the 15° , 30° , and 45° triangle components, where some topologies exhibited much greater maximum displacements compared to others. The fillet components showed the most obvious

differences, with variations in maximum nodal displacement of up to 0.2 mm between certain topologies. In contrast, the cube components did not display this trend as strongly, suggesting that the sensitivity to topology may be more pronounced in certain geometric configurations. These findings indicate that while the average structural response may be relatively insensitive to topology, the choice of topology can have a significant impact on the localized maximum displacements in specific regions of the structure. This information may be valuable for design optimization efforts that prioritize limiting peak displacements or stresses in critical areas.

One final note before finishing this section. When the parameters of geometry were varied according to the tables in Chapter 1.6.2, some of the resulting topologies were very similar to each other, and others were deemed to be undesirable, due to very small thin supports. These repeated and faulty topologies were discarded and were not used for the manufacturing simulation. This resulted in different groups being used for each geometry study, as can be seen in the members of each graph.

Graphs summarizing these results are shown below. Figure 4.2 show the results for the cubic component. Figures 4.3, 4.4, and 4.5 show the results for all the triangular components, while Figures 4.6, 4.7, and 4.8 show the results of the components with fillets. Each of the bars in the figures below represents a particular combination of parameters belonging to a topology resulting from the COMSOL simulation. Figure 4.1 explains what each x-axis label means. The parameters shown in the key are the same parameters explained in Table 1.2.

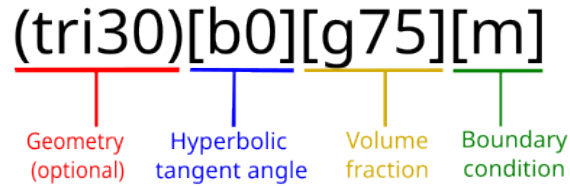


Figure 4.1: Topology key explanation.

In summary, the results of these simulations suggest that varying the objective function parameters in the COMSOL simulations did not result in any noticeable differences

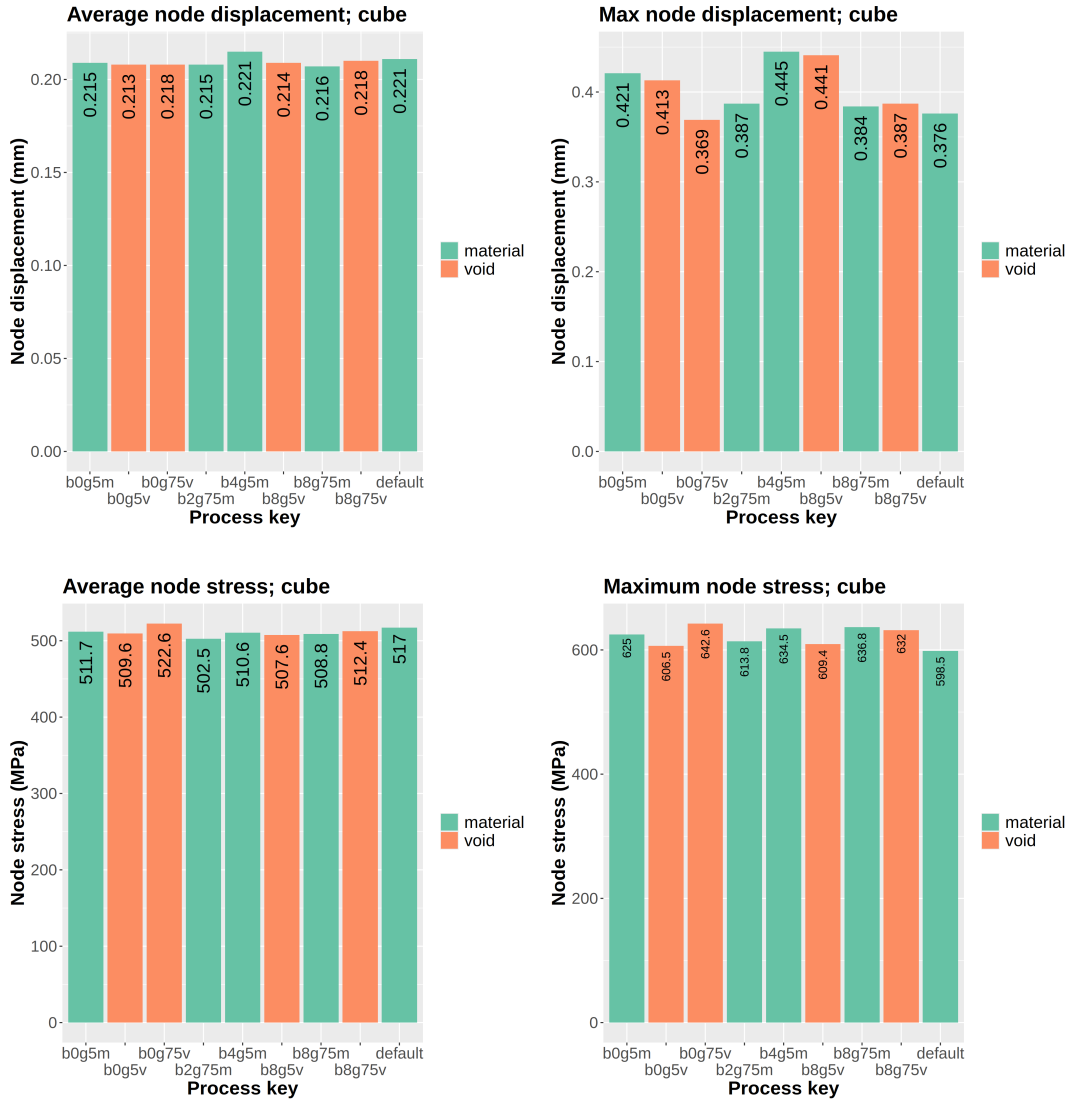


Figure 4.2: Results of cube.

in the resulting topologies. This suggests that the choice of objective function had little impact on the final structural configurations. Upon closer examination, it was found that the thermal compliance, rather than the mechanical compliance, was the dominant factor driving the topology optimization. This indicates that for the given loading conditions, where the primary load is the weight of the component itself, the mechanical compliance does not play a significant role in the optimization process. The thermal effects appear to be the governing factor, likely due to the relatively low magnitude of the

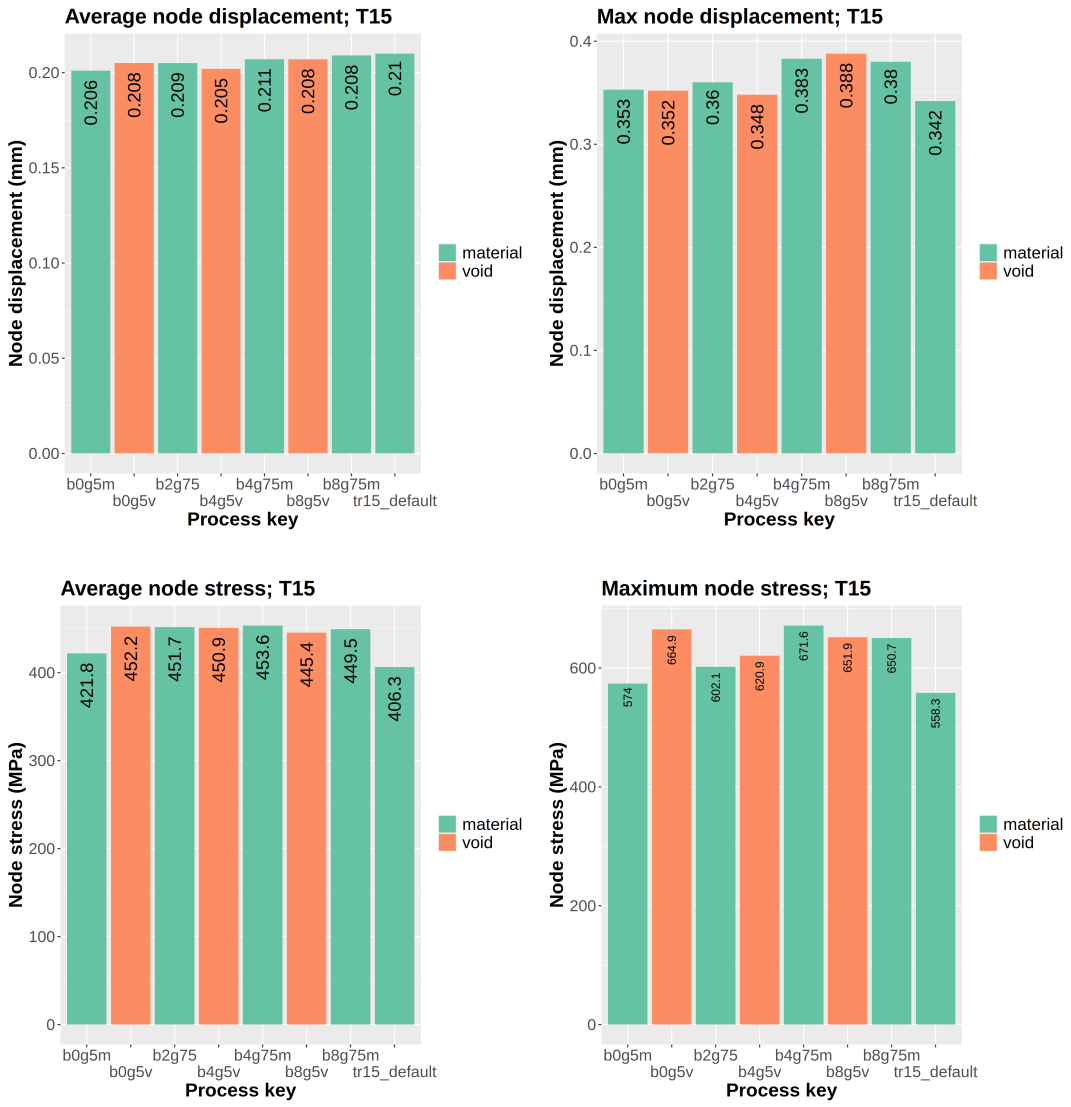


Figure 4.3: Results of 15° triangle.

mechanical loads. These findings suggest that a multi-objective function approach may not be necessary for this particular study, as the thermal compliance alone seems to be the primary driver of the optimal topologies. This simplification could be advantageous for future design optimization efforts, as it reduces the complexity of the problem and allows for a more focused exploration of the thermal-driven structural behavior.

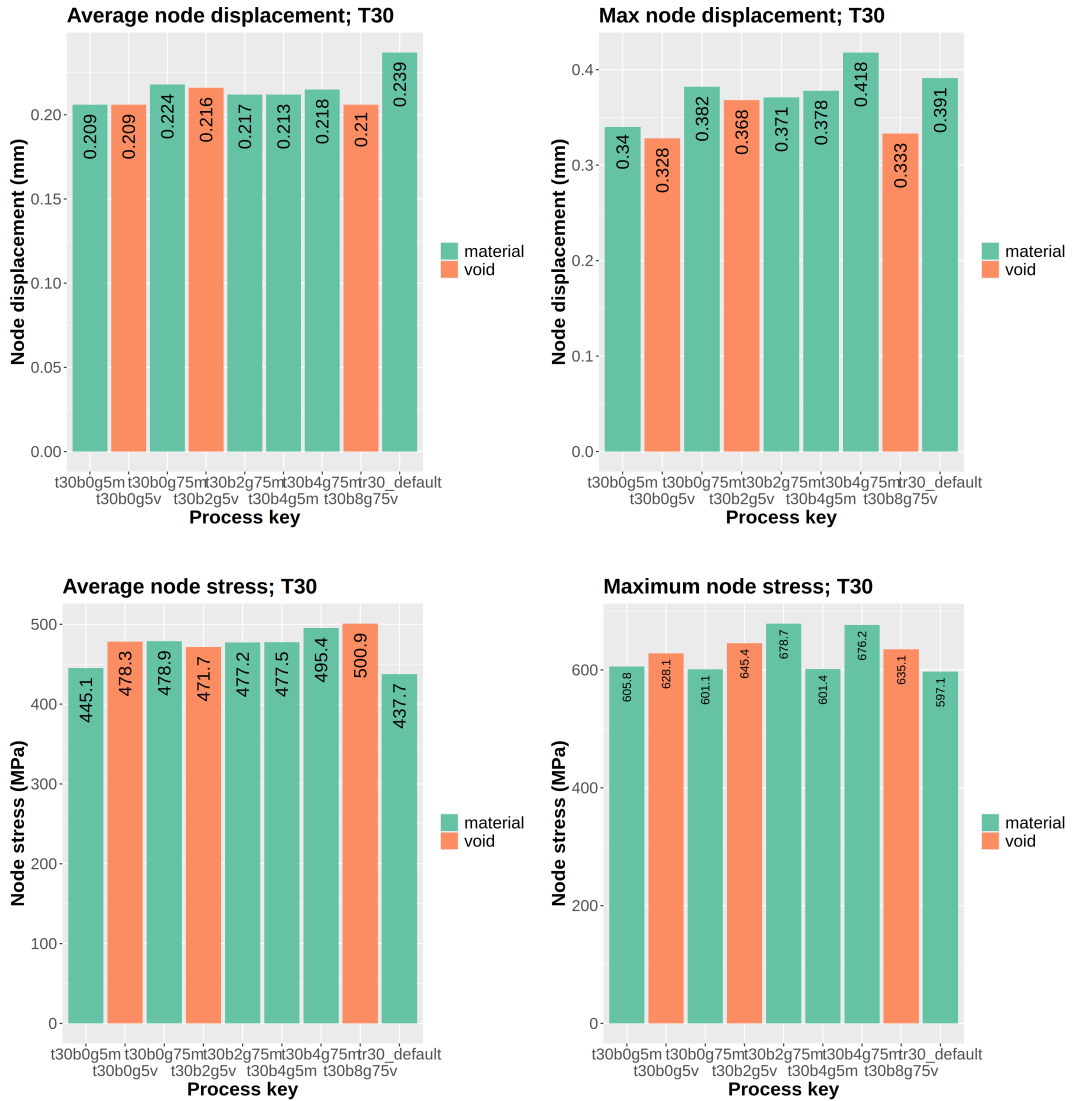


Figure 4.4: Results of 30°triangle.

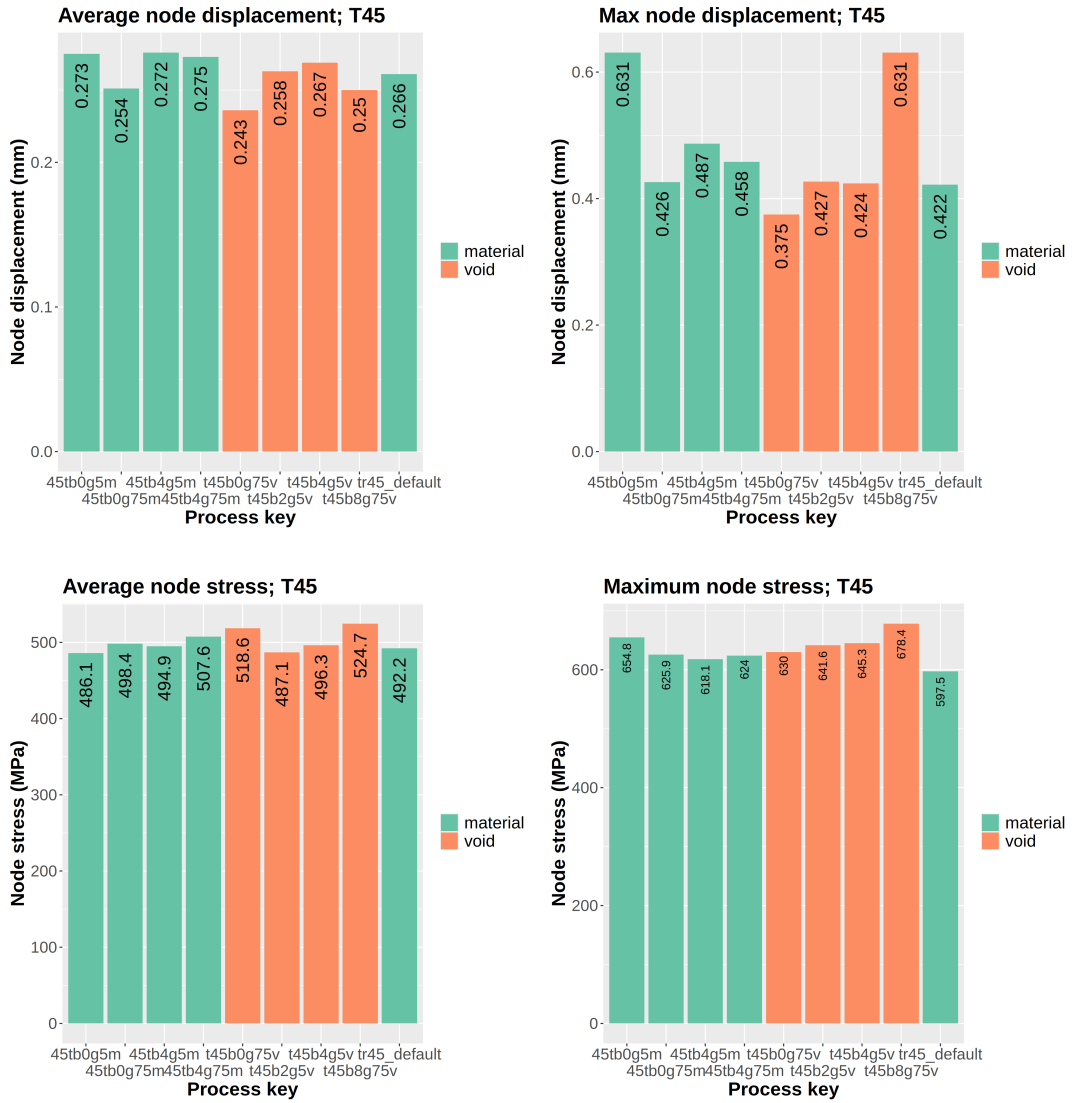


Figure 4.5: Results of 45° triangle.

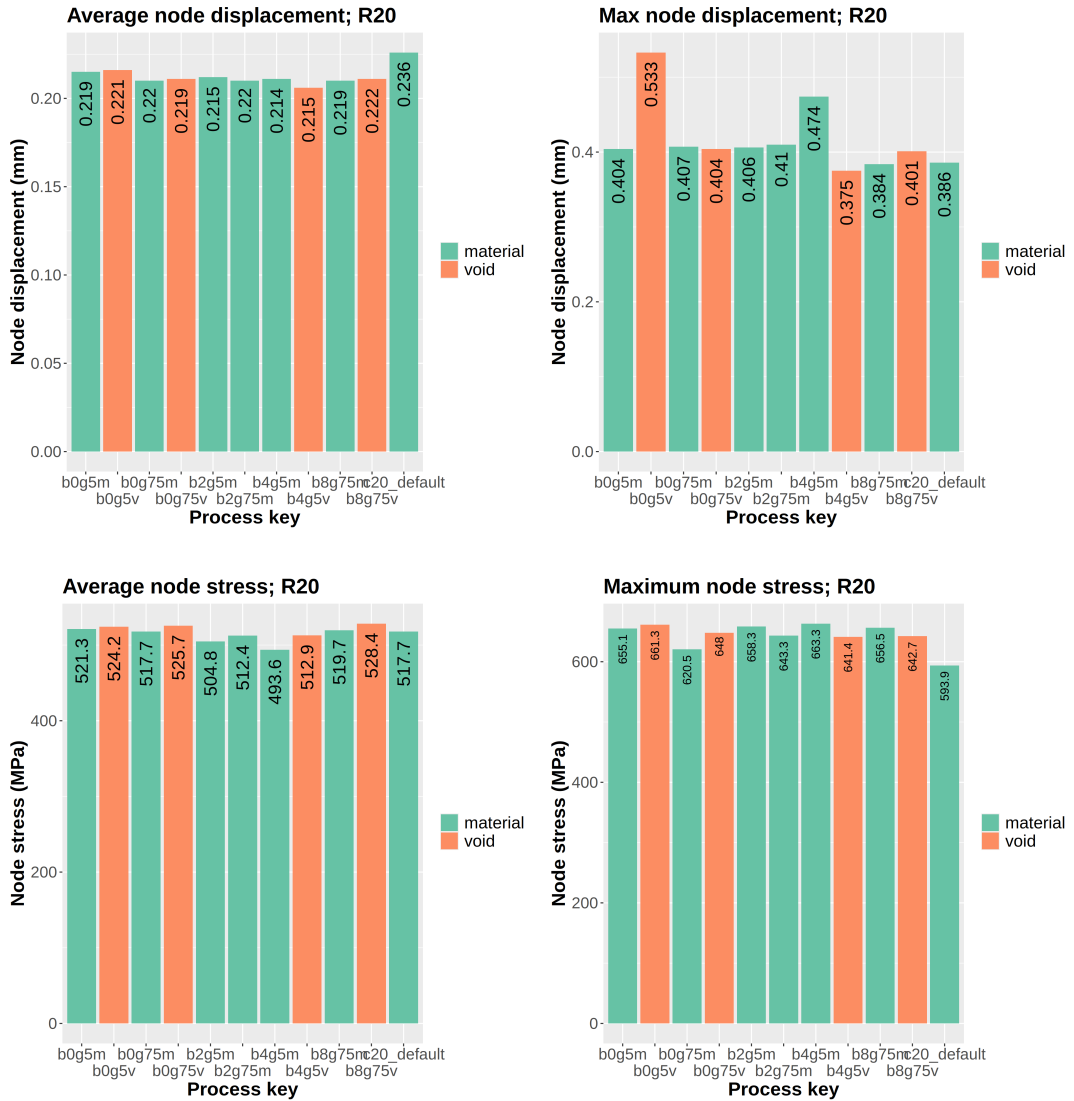


Figure 4.6: Results of 20R fillet.

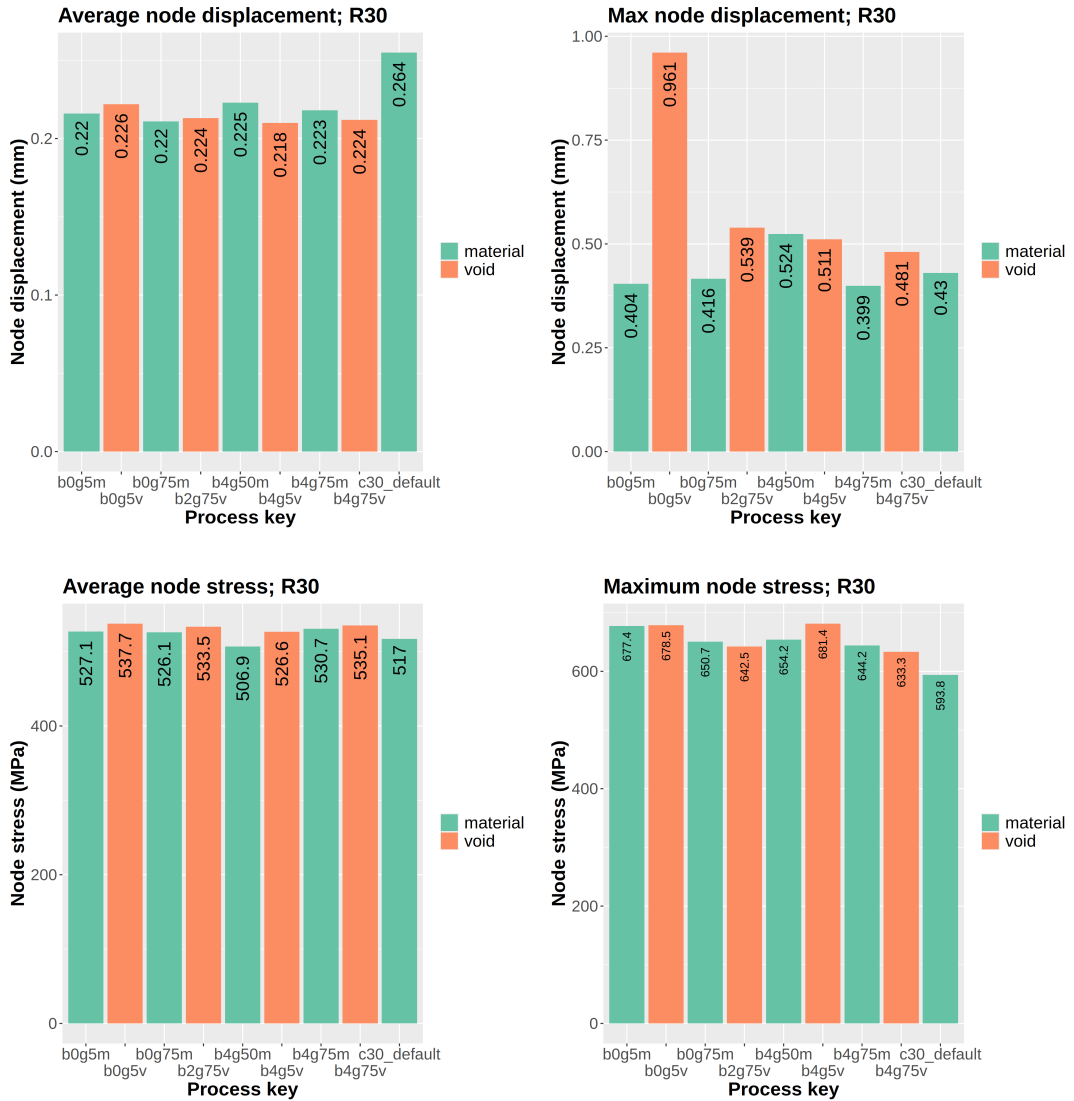


Figure 4.7: Results of 30R fillet.

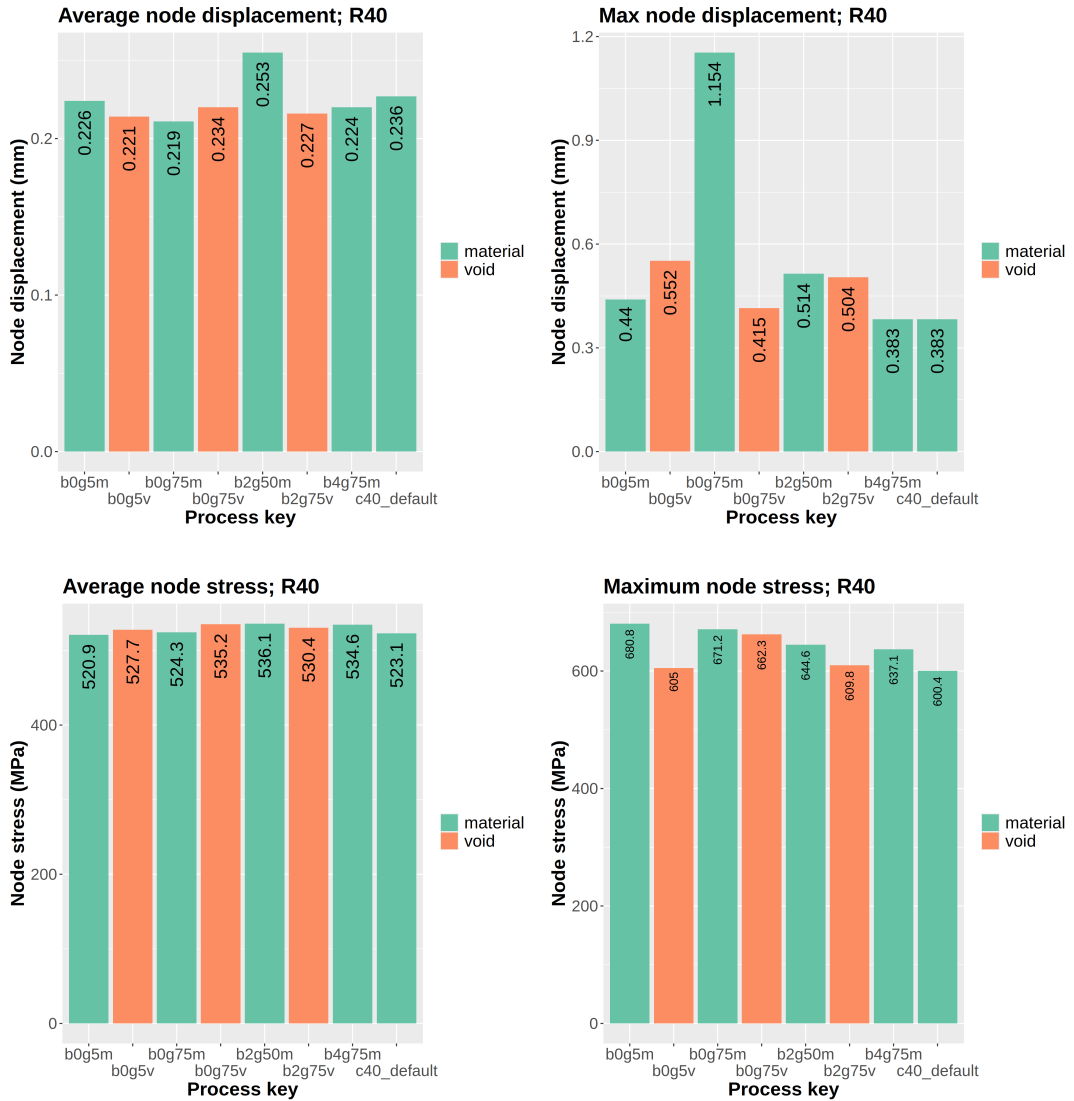


Figure 4.8: Results of 40R fillet.

4.2 Results of femoral components

4.2.1 Displacement analysis

For the displacement analysis of the femoral component, statistics on the surface mesh of the simulation results were computed. From this graph,

Figure 4.9 shows the distribution of the surface nodal displacements of the femoral component. The utility of this graph is to visualize easily how the displacements of each result are distributed. We see that the distribution is asymmetrical and it does not resemble a normal distribution. From the other graphs, it can also be observed that the hyperbolic tangent variation within volume fraction group creates slight differences in the distribution of nodal displacements, although it seems only to occur in some particular cases. Lastly, it can be seen from these graphs that the lower volume fractions of 25% and 33% have slightly thicker right-end tails, suggesting that there is a greater number of nodes with high displacement as compared to the other simulations.

This trend can be more easily visualized by computing the average nodal deformation for each case. The left graph of Figure 4.10 shows the average nodal deformation, where each column corresponds to a simulation result and each color represents a particular volume fraction group. It is clear from this graphs that the 25% and 33% volume fraction results exhibit a slightly larger average deformation compared to the rest of the simulations. This is more clearly show in the right figure, which shows the average deformation for each volume fraction group as a whole. Nevertheless, this difference between average nodal deformation could still be attributed to the numerical uncertainty due to voxelization, as it had been previously established that the numerical errors of the simulation could account up to a variability of 0.01mm.

Next, the maximum nodal displacements of each group were computed. The results are shown in Figure 4.11. There are three results that show excessive deformation at a few nodes. Additionally, it was noticed during the simulation that some voxels exhibited abnormal behavior, and deformed in a non-physical manner. This is showcased in

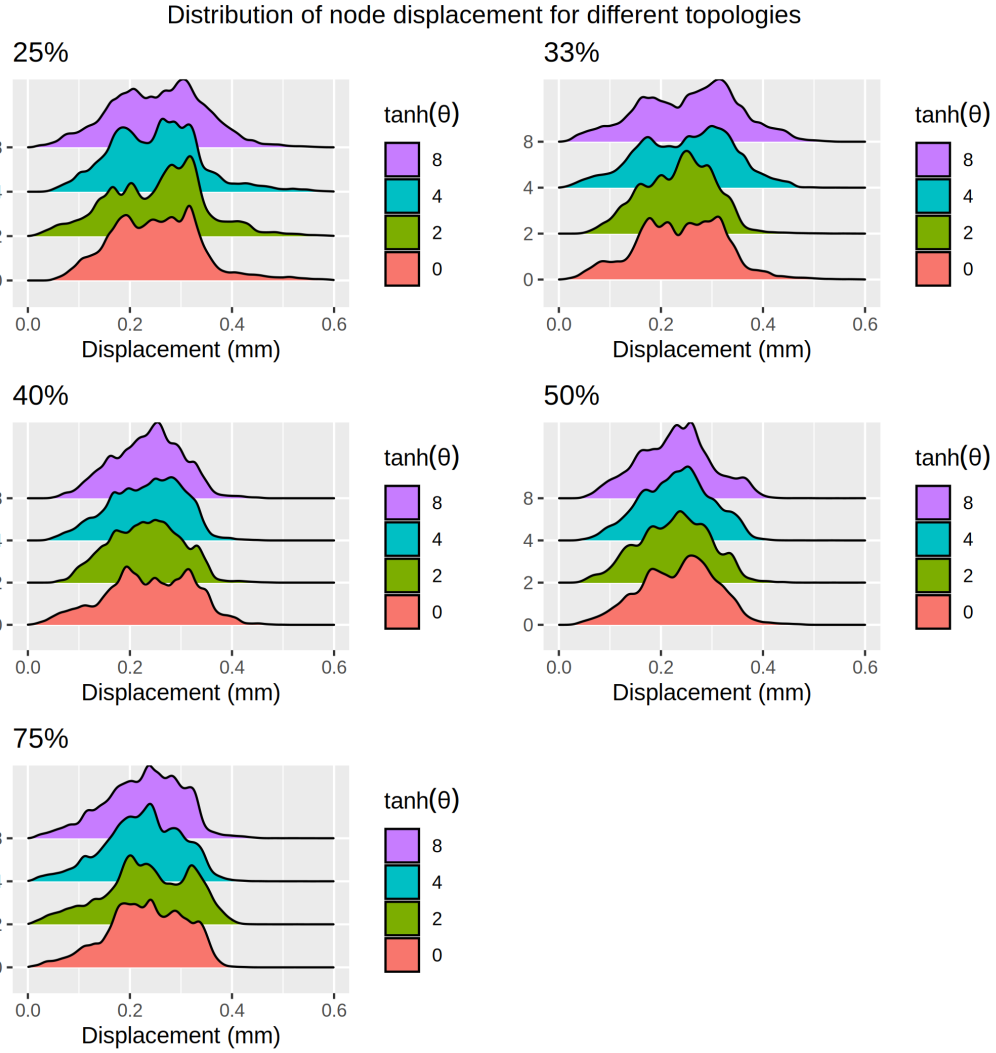


Figure 4.9: Density distribution of nodal displacements, grouped by volume fraction and hyperbolic tangent angle.

Figure 4.12, where one voxel has merged into a neighboring one. Therefore, it is highly suspected that the results for these geometries show faulty node displacements caused by a bug or anomaly in the finite element calculation. To determine whether these excessive deformations are significant, the deformation were binned in bins of 0.1 mm. The result of this operation is shown in Table 4.1.

Table 4.1 shows that there are some ranges of deformation that do not contain any nodes, meaning that there are discontinuities in the nodal deformations. This behavior is clearly non-physical, and suggests that these offending nodes should be

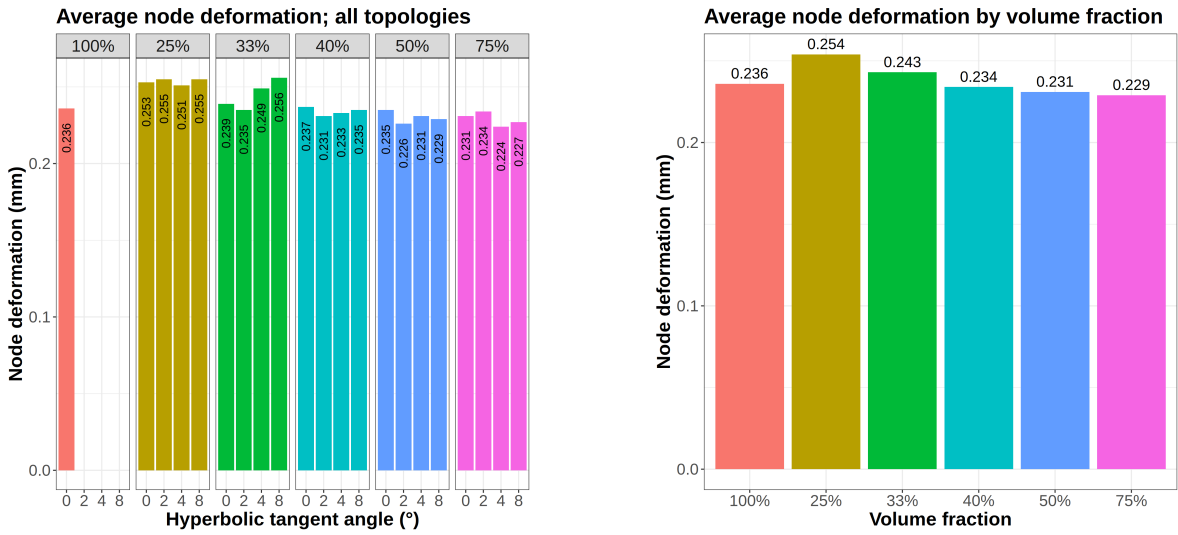


Figure 4.10: Average nodal displacement for femoral component simulations. The left graph shows the average deformation for each topology investigated, the right graph shows the average deformation of topologies when grouped by volume fraction.

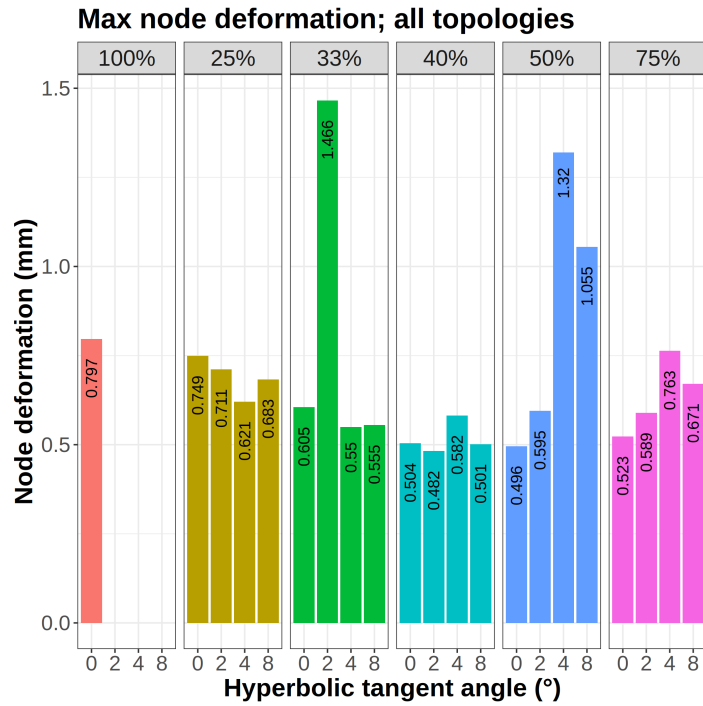


Figure 4.11: Maximum nodal displacements for the femoral component simulations. Notice that there are three topologies that show an excessive maximal displacement. These displacements are very likely to be outliers, and further analysis was done to understand their nature.

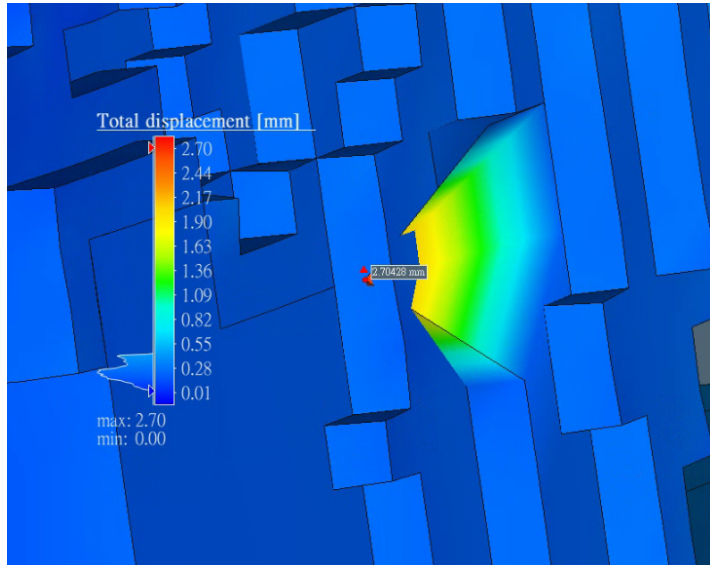


Figure 4.12: Screenshot of abnormal voxel behavior from simulation result. The voxel seems to be deformed and merging inside the structure itself. Luckily, only a handful of voxels of these sort exist, with the rest of the geometry showing much more sensible results.

discarded. To discard them, all nodes further away from three standard deviation were deleted from these topologies, and the statistics were recalculated. The graph of the maximum nodal displacements with corrected distributions are shown in Figure 4.13. From this corrected figure it can be seen that there is local minima in the maximum nodal deformation for the results of the 40% volume fraction simulations. Additionally, the differences between groups is much greater than the numerical uncertainty from the variation due to voxelization (> 0.011 mm), making this result significant. Therefore, we can infer from this data that variation in topology does not result in a big effect on average node deformation, but can have an impact on the maximum node deformation of the resulting structure.

Lastly, all of the following trends can be succinctly visualized using a box and whisker plot, shown in Figure 4.14. From this final plot we can see once more that the average deformation stays constant throughout, but that there is a local minimum in the maximum deformation in the groups with intermediate volume fractions. The full statistics of the nodal displacements are shown in Table 4.2.

Table 4.1: Bins of nodal displacement for suspicious results. The bins labeled with an asterisk have very little to no members, indicating a discontinuous nodal deformation distribution. This is deemed to be non-physical and likely an error with the finite element result.

g33b2		g50b4		g50b8	
bin	percentage	bin	percentage	bin	percentage
[0,0.1]	2.532%	[0,0.1]	2.883%	[0,0.1]	3.850%
(0.1,0.2]	29.005%	(0.1,0.2]	29.626%	(0.1,0.2]	30.144%
(0.2,0.3]	50.515%	(0.2,0.3]	50.408%	(0.2,0.3]	50.650%
(0.3,0.4]	17.192%	(0.3,0.4]	16.847%	(0.3,0.4]	14.992%
(0.4,0.5]	0.658%	(0.4,0.5]	0.197%	(0.4,0.5]	0.326%
(0.5,0.6]	0.076%	(0.5,0.6]	0.019%	(0.5,0.6]	0.021%
(0.6,0.7]*	0.002%	(0.6,0.7]	0.010%	(0.6,0.7]	0.011%
(0.7,0.8]	0.007%	(0.7,0.8]*	0.000%	(0.7,0.8]*	0.000%
(0.8,0.9]*	0.002%	(0.8,0.9]*	0.002%	(0.8,0.9]*	0.000%
(0.9,1]*	0.003%	(0.9,1]	0.005%	(0.9,1]*	0.004%
(1,2]	0.009%	(1,2]*	0.002%	(1,2]*	0.002%
TOTAL	100.00%	TOTAL	100.00%	TOTAL	100.000%

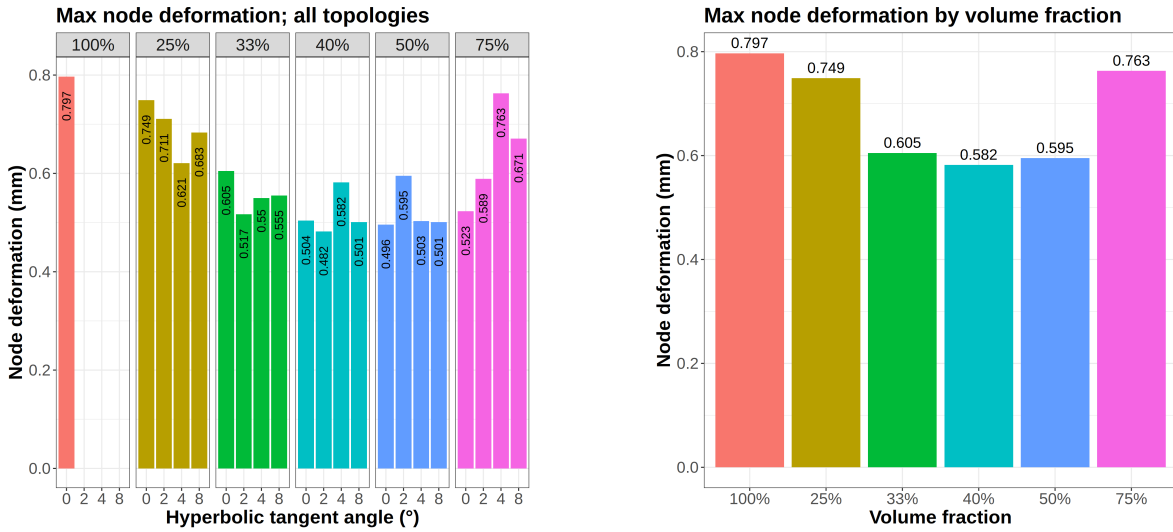


Figure 4.13: Maximum nodal displacement after corrections.

Based on the node displacement analysis conducted for this support structure configuration, we have identified an optimal geometric arrangement characterized by a 40% volume fraction and a hyperbolic tangent angle of 2 degrees. The empirical evidence demonstrates a non-linear relationship between structural performance and volume fraction, wherein both excessively high and low volume fractions correlate with elevated average node displacement values. This finding suggests that deformation minimiza-

tion can be achieved through the implementation of intermediate volume fraction parameters. Additionally, just as the simple geometry study, the current displacement analysis is unable to find any strong relationship between hyperbolic angle and average or maximum node deformation. Nevertheless, it is still suggested to perform systematic variation of hyperbolic angle when designing support structures. The analysis reveals that even within groups of identical volume fractions, there are still specific angular values that yield optimal performance as measured by maximum node deformation.

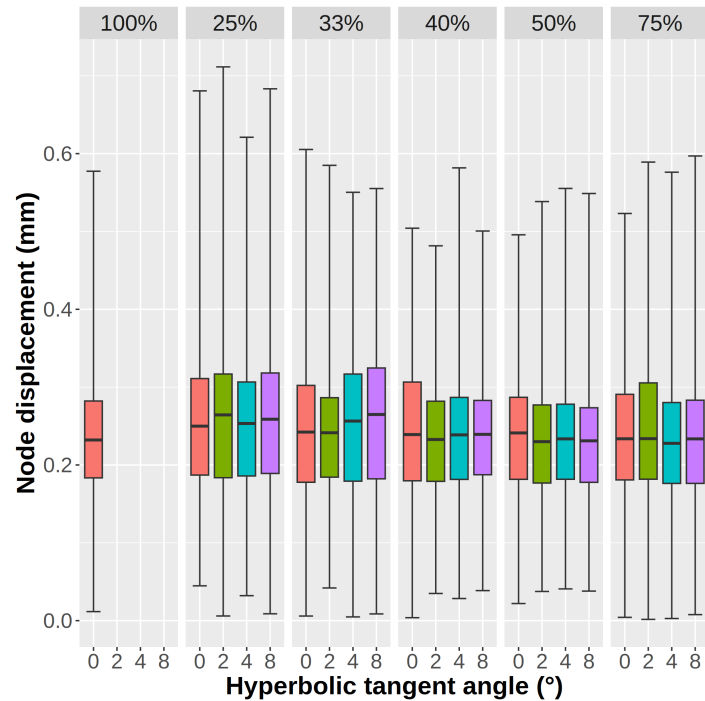


Figure 4.14: Box and whisker plot for femoral displacement of all topologies.

Table 4.2: Statistics of nodal displacements (mm); all topologies

PROCESS	VOLUME_FACTOR	TANH_ANGLE	average	median	stdev	maximum
g100b0	100%	0	0.236	0.232	0.073	0.797
g25b0	25%	0	0.253	0.250	0.091	0.749
g25b2	25%	2	0.255	0.264	0.097	0.711
g25b4	25%	4	0.251	0.253	0.088	0.621
g25b8	25%	8	0.255	0.259	0.091	0.683
g33b0	33%	0	0.239	0.242	0.086	0.605
g33b2	33%	2	0.235	0.241	0.071	1.466
g33b4	33%	4	0.249	0.256	0.090	0.550
g33b8	33%	8	0.256	0.265	0.096	0.555
g40b0	40%	0	0.237	0.239	0.086	0.504
g40b2	40%	2	0.231	0.233	0.069	0.482
g40b4	40%	4	0.233	0.239	0.071	0.582
g40b8	40%	8	0.235	0.239	0.068	0.501
g50b0	50%	0	0.235	0.241	0.074	0.496
g50b2	50%	2	0.226	0.230	0.070	0.595
g50b4	50%	4	0.232	0.234	0.069	1.320
g50b8	50%	8	0.229	0.231	0.072	1.055
g75b0	75%	0	0.231	0.234	0.076	0.523
g75b2	75%	2	0.234	0.234	0.085	0.589
g75b4	75%	4	0.224	0.228	0.075	0.763
g75b8	75%	8	0.227	0.234	0.076	0.671

4.2.2 Stress analysis

To analyze the differences in internal stresses caused by the topologies, we inspect the node stress density distributions. In contrast with the displacement density distribution, there is very little variability between groups. On the other hand, across groups we can see differences in the spread of stress. For example, the stress are most densely concentrated around the peak of the 25% group compared to the groups with higher volume fractions, such as 50% and 75%. This indicates that some groups have smaller standard deviations, with values more closely packed together. This can be confirmed by looking at the statistics in Table 4.3, where we can see slight differences in the standard deviation of topologies.

Next, we inspect the average deformation of the simulation results. We can see that the baseline case has the smallest average stresses, but as soon as topologies with lower volume fraction are used, the average stresses rises more than 20%, from a baseline value of 400 MPa to over 485 MPa. The average stress does not change considerably from topology to topology, which is similar to what was noticed for the average nodal displacement. This trend is shown in Figure 4.16. Looking at the maximum stress yields a very interesting result; namely, that all of the topologies have a near constant maximum stress. This result is clear from looking at both graphs in Figure 4.17.

Lastly, the box-whisker plot of Figure 4.18 shows a succinct summary of all the statistics discussed in this section.

The stress analysis results was not able to reveal any correlations between both volume fraction and nodal stress, as well as between hyperbolic tangent angle and nodal stress. This is an anomalous finding, given that all simulations produced remarkably consistent maximum stress values with minimal variations in standard deviation and average nodal stresses across configurations. The homogeneity of stress results across all the different supporting structure geometries might be an indication of methodological issues in the simulation approach or computational limitations in the finite element software. These suspiciously uniform outcomes warrant further investigation.

A more comprehensive stress analysis approach would involve examining the spatial distribution and concentration of stresses throughout the entire three-dimensional structure, rather than relying solely on statistical measures of nodal stress. By generating detailed stress field maps, researchers could identify critical high-stress regions, stress gradients, and potential failure initiation points within the support structure. This methodology would provide more meaningful insights into the structural behavior and better illuminate the relationships between geometric parameters (volume fraction and hyperbolic tangent angle) and mechanical performance. Such visualization-based analysis would likely reveal patterns and correlations that were obscured by the aggregate statistical approach, thereby offering more valuable guidance for future support structure optimization.

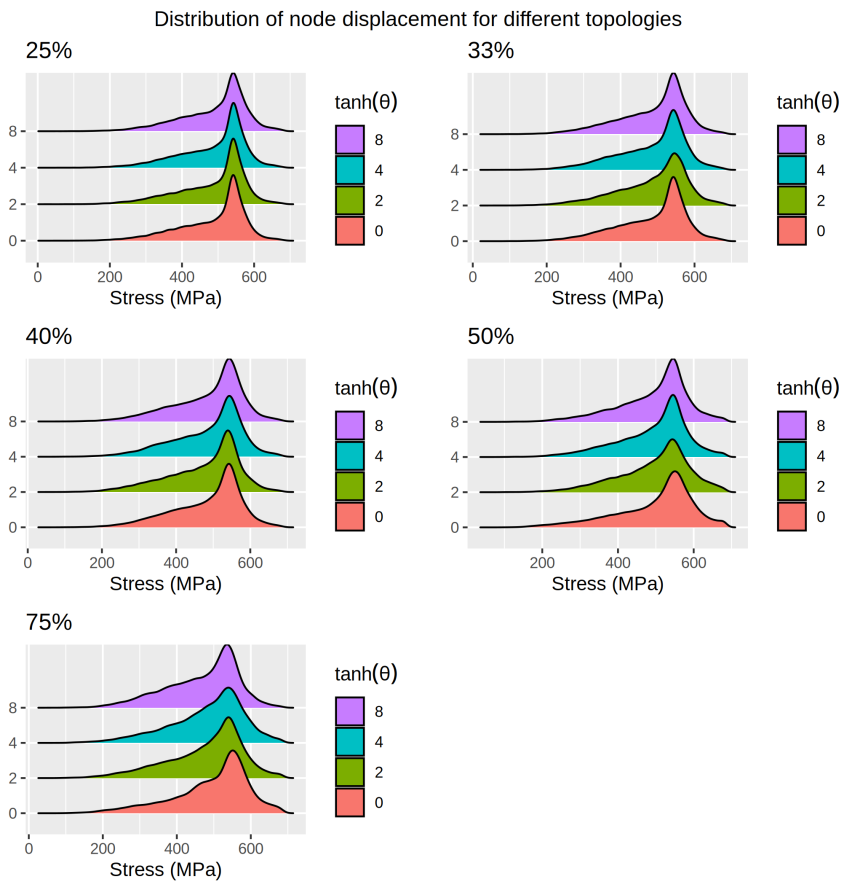


Figure 4.15: Distribution of node stresses of support structures for femoral component.

Table 4.3: Statistics of nodal stresses (MPa); all topologies.

process	volfrac	tanh	average	median	stdev	maximum
g100b0	100%	0	400.712	400.543	125.462	681.564
g25b0	25%	0	488.693	521.220	90.780	682.397
g25b2	25%	2	487.813	521.155	92.320	682.452
g25b4	25%	4	489.154	520.744	91.062	682.067
g25b8	25%	8	491.847	520.078	90.308	682.278
g33b0	33%	0	488.277	517.976	92.675	682.381
g33b2	33%	2	489.542	513.752	94.154	682.249
g33b4	33%	4	486.927	514.574	93.063	682.344
g33b8	33%	8	489.056	516.796	92.293	682.475
g40b0	40%	0	485.939	512.923	92.540	682.106
g40b2	40%	2	477.902	504.982	96.052	682.617
g40b4	40%	4	487.494	513.938	93.282	682.469
g40b8	40%	8	488.478	516.430	93.060	682.305
g50b0	50%	0	499.355	528.665	102.975	682.169
g50b2	50%	2	497.140	517.544	94.278	682.090
g50b4	50%	4	493.977	518.358	93.099	681.940
g50b8	50%	8	495.033	519.732	92.447	682.037
g75b0	75%	0	494.405	521.447	102.529	682.077
g75b2	75%	2	479.523	504.079	101.771	682.086
g75b4	75%	4	482.653	503.432	100.233	682.198
g75b8	75%	8	469.531	493.421	97.234	681.919

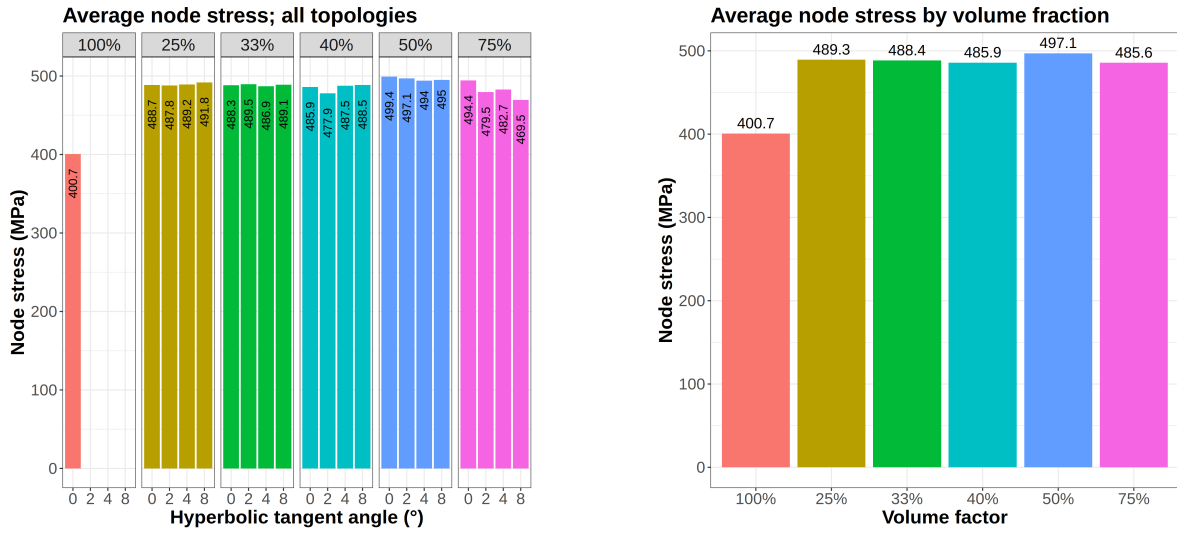


Figure 4.16: Average node stress for supporting structure of femoral component.

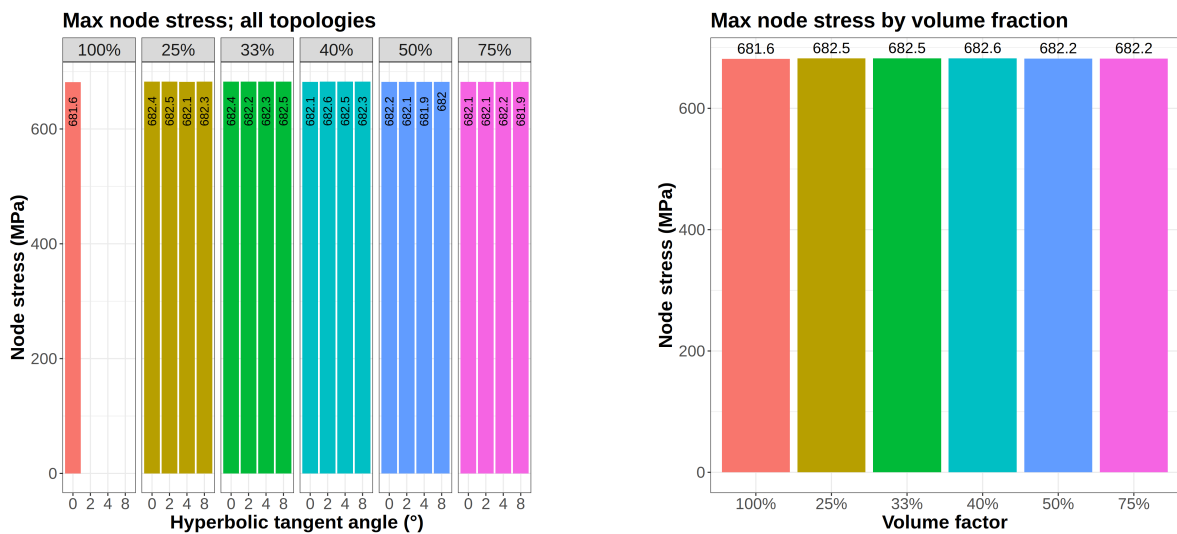


Figure 4.17: Maximum node stress for supporting structure of femoral component.

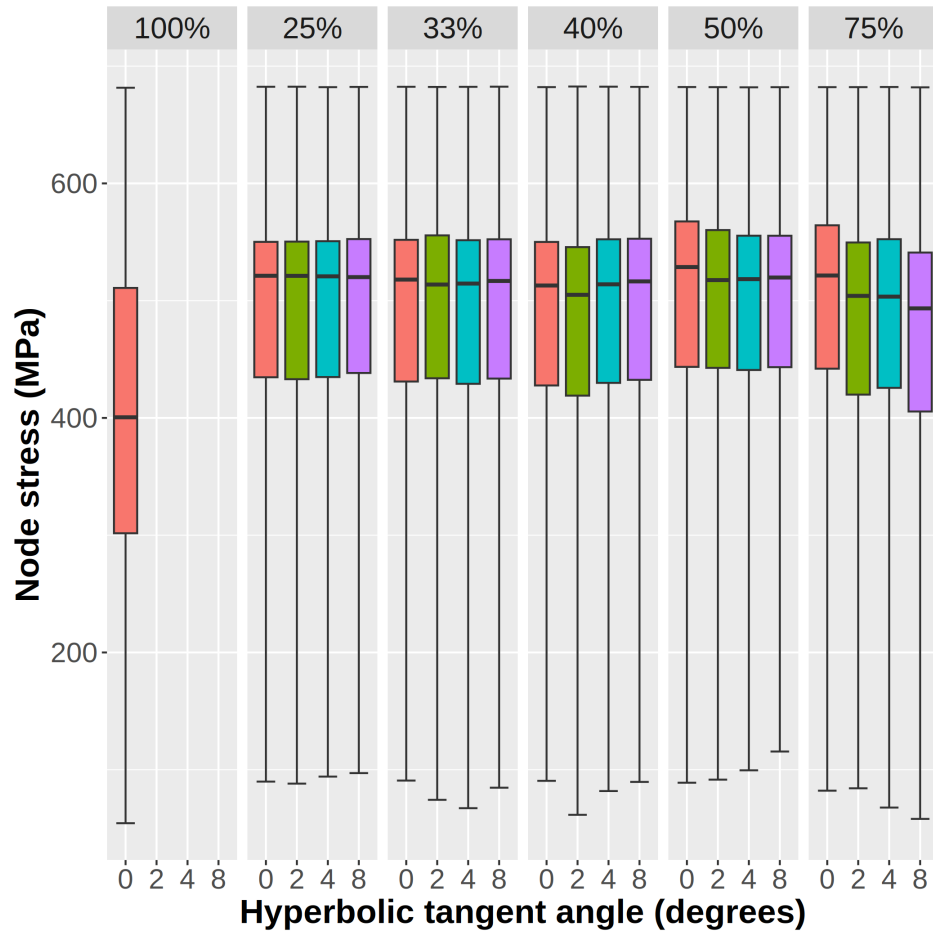


Figure 4.18: Box-and-whisker plot of nodal stress values of topologies of femoral component.

5. Discussion and conclusions

5.1 Conclusions

1. The findings of this study demonstrate the efficacy of topology optimization in reducing the volume of supporting structures while minimizing the overall deformation of the component. The results indicate that the judicious selection of optimal topologies can play a significant role in mitigating the maximum deformation experienced by the component. This phenomenon may be attributed to the principle that the total thermal expansion is proportional to the amount of material present. Topologies that minimize the volume of the supporting structure could potentially reduce the total thermal expansion, leading to lower maximum deformations.
2. Furthermore, the investigation reveals that excessively reducing the volume fraction of the supporting structure may be detrimental to the thermal deformation performance, when using maximum displacement as a performance metric. The study of the maximum nodal deformation of the femoral component showed that excessive volume fraction reduction led to high maximum deformations. This observation leads to the hypothesis that a reduction in material volume can hinder the heat transfer pathways, creating higher thermal gradients within the structure and resulting in increased thermal expansion.
3. The results from the simple geometric configurations suggest that the hyperbolic tangent angle and variation of boundary conditions are not directly correlated with the overall deformation and stress of the structure. Additionally, the analysis indicates that mechanical compliance has a negligible effect on the observed

outcomes, as the dominant physical phenomenon governing the system appears to be thermal transfer rather than mechanical loading. This is likely due to the relatively low magnitude of the mechanical loads, which are primarily driven by the weight of the component itself.

4. Overall, the insights gained from this study highlight the potential of topology optimization to enhance the design of supporting structures, balancing the competing objectives of material reduction and thermal deformation control. The understanding of the underlying physical mechanisms, such as the role of thermal expansion and heat transfer, can guide the development of more efficient and reliable structural designs. In particular, in this study it was observed that mechanical compliance was not influential, but this methodology could still be applied to other systems where the boundary loads might have a bigger influence, such as loads and stresses encountered in heat exchangers or turbomachinery.

5.2 Future research

Here are some ideas that could be developed in future research to improve and refine the current method and address some of its deficiencies:

1. One potential area of improvement is the integration of topology optimization with lattice structures. By merging these two design strategies, it may be possible to achieve even greater reductions in the volume of the supporting structure while maintaining the desired deformation characteristics. The use of lattice structures could introduce additional design flexibility and potentially lead to further material savings.
2. Additionally, a crucial aspect of accurate thermomechanical simulation is the proper calibration of thermal parameters. Unfortunately, the standard operating procedures for obtaining the correct thermal calibration parameters are not well-defined, and this can be a challenging task. In the current study, the thermal

calibration was not accounted for, which means that while the general trends observed are likely accurate, the specific numerical values of displacements and stresses may not fully reflect realistic conditions. To ensure a more precise prediction of the component's behavior, future studies should prioritize the careful calibration of thermal parameters, following established or newly developed protocols. This additional step would help confirm that the results obtained are truly representative of the expected real-world performance.

3. In addition to the statistical analysis of average and maximum values, the current study could be enhanced by incorporating a more comprehensive 3D visualization approach. By layering the displacement and stress distributions directly onto the 3D geometry of the component, it would be possible to gain a deeper understanding of the spatial distribution of deformation and stress within the structure. This level of detail could provide insights into the specific regions experiencing the highest levels of deformation and stress, which may not be readily apparent from the summary statistics alone.
4. Continuing from the previous point, comparing the 3D visualization results with the original CAD model could pinpoint the critical areas that require particular attention. Identifying these high-stress or high-deformation regions could inform post-processing decisions, such as targeted machining or reinforcement, to optimize the final design and reduce manufacturing costs. Additionally, this detailed spatial analysis may lead to a better understanding of the underlying design factors that contribute to the observed deformation patterns, guiding future iterations of the topology optimization process.
5. Future research should prioritize a comprehensive reexamination of the stress analysis methodology, including mesh sensitivity studies, alternative solver approaches, and verification against physical testing. This is due to the counterintuitive results from the nodal displacement and stress analyses, in which there were clear differences in nodal displacements between geometries, but the stress values

were suspiciously similar throughout all geometries. This incongruence between the displacement analysis and the stress analysis requires more attention to establish more reliable stress prediction mechanisms for optimized support structure design.

References

- [1] M. A. Varacallo, T. D. Luo, A. Mabrouk, and N. A. Johanson, “Total Knee Arthroplasty Techniques,” in *StatPearls*, Treasure Island (FL): StatPearls Publishing, 2025. pmid: 29763071. Accessed: Feb. 11, 2025. [Online]. Available: <http://www.ncbi.nlm.nih.gov/books/NBK499896/>.
- [2] “Elderly and disadvantaged situation, trend and strategy analysis of living environment in Taiwan,” Architecture and Building Research Institute, Ministry of the Interior, ROC (Taiwan), Accessed: Feb. 11, 2025. [Online]. Available: http://www.abri.gov.tw/en/News_Content.aspx?n=908&s=317737&sms=9518.
- [3] F.-H. Lin et al., “The increase in total knee replacement surgery in Taiwan,” *Medicine*, vol. 97, no. 31, e11749, Aug. 3, 2018, ISSN: 0025-7974. DOI: 10.1097/MD.00000000000011749. pmid: 30075592. Accessed: Feb. 11, 2025. [Online]. Available: <https://www.ncbi.nlm.nih.gov/pmc/articles/PMC6081077/>.
- [4] S. P. Narra, P. N. Mittwede, S. DeVincent Wolf, and K. L. Urisch, “Additive Manufacturing in Total Joint Arthroplasty,” *The Orthopedic clinics of North America*, vol. 50, no. 1, pp. 13–20, Jan. 2019, ISSN: 0030-5898. DOI: 10.1016/j.occl.2018.08.009. pmid: 30477702. Accessed: Feb. 11, 2025. [Online]. Available: <https://www.ncbi.nlm.nih.gov/pmc/articles/PMC6555404/>.
- [5] A. D. Valino, J. R. C. Dizon, A. H. Espera, Q. Chen, J. Messman, and R. C. Advincula, “Advances in 3D printing of thermoplastic polymer composites and nanocomposites,” *Progress in Polymer Science*, vol. 98, p. 101162, Nov. 1, 2019, ISSN: 0079-6700. DOI: 10 . 1016 / j . progpolymsci . 2019 . 101162. Accessed: Feb. 27, 2025. [Online]. Available: <https://www.sciencedirect.com/science/article/pii/S0079670018303976>.

- [6] M. Marsh and S. Newman, “Trends and developments in hip and knee arthroplasty technology,” *Journal of Rehabilitation and Assistive Technologies Engineering*, vol. 8, p. 2 055 668 320 952 043, Feb. 8, 2021, ISSN: 2055-6683. DOI: 10 . 1177 / 2055668320952043. pmid: 33614108. Accessed: Feb. 17, 2025. [Online]. Available: <https://www.ncbi.nlm.nih.gov/pmc/articles/PMC7874345/>.
- [7] M. H. Mobarak et al., “Recent advances of additive manufacturing in implant fabrication –A review,” *Applied Surface Science Advances*, vol. 18, p. 100 462, Dec. 1, 2023, ISSN: 2666-5239. DOI: 10 . 1016/j.apsadv.2023.100462. Accessed: Feb. 17, 2025. [Online]. Available: <https://www.sciencedirect.com/science/article/pii/S266652392300096X>.
- [8] K. Pathak et al., “3D printing in biomedicine: Advancing personalized care through additive manufacturing,” *Exploration of Medicine*, vol. 4, no. 6, pp. 1135–1167, 6 Dec. 29, 2023, ISSN: 2692-3106. DOI: 10 . 37349 / emed . 2023 . 00200. Accessed: Feb. 17, 2025. [Online]. Available: <https://www.explorationpub.com/Journals/em/Article/1001200>.
- [9] A. M. Jonaet, H. S. Park, and L. C. Myung, “Prediction of residual stress and deformation based on the temperature distribution in 3D-printed parts,” *The International Journal of Advanced Manufacturing Technology*, vol. 113, no. 7, pp. 2227–2242, 7 Apr. 1, 2021, ISSN: 1433-3015. DOI: 10 . 1007 / s00170 - 021 - 06711 - 5. Accessed: Mar. 1, 2025. [Online]. Available: <https://link-springer-com.proxyone.lib.nchu.edu.tw:8443/article/10 . 1007 / s00170 - 021 - 06711 - 5>.
- [10] R. E. Laureijs and J. B. Rocca. “Metal Additive Manufacturing: Cost Competitive Beyond Low Volumes | J. Manuf. Sci. Eng. | ASME Digital Collection,” Accessed: Feb. 11, 2025. [Online]. Available: <https://asmedigitalcollection.asme.org/manufacturingscience/article/139/8/081010/376354/Metal-Additive-Manufacturing-Cost-Competitive>.

- [11] Chung, Pei-Hsu, “Study on the Lattice Support Structures to Minimize Thermal Distortion in Selective Laser Melting Using Simulation and Design of Experiments,” 國立中興大學, 臺中市, 2024.
- [12] G. Allaire and B. Bogosel, “Optimizing supports for additive manufacturing,” *Structural and Multidisciplinary Optimization*, vol. 58, no. 6, pp. 2493–2515, 6 Dec. 1, 2018, ISSN: 1615-1488. DOI: 10.1007/s00158-018-2125-x. Accessed: Feb. 20, 2025. [Online]. Available: <https://link-springer-com.proxyone.lib.nchu.edu.tw:8443/article/10.1007/s00158-018-2125-x>.
- [13] Y.-H. Kuo, C.-C. Cheng, Y.-S. Lin, and C.-H. San, “Support structure design in additive manufacturing based on topology optimization,” *Structural and Multidisciplinary Optimization*, vol. 57, no. 1, pp. 183–195, 1 Jan. 1, 2018, ISSN: 1615-1488. DOI: 10.1007/s00158-017-1743-z. Accessed: Feb. 20, 2025. [Online]. Available: <https://link-springer-com.proxyone.lib.nchu.edu.tw:8443/article/10.1007/s00158-017-1743-z>.
- [14] H. A. Kumar, P. F. Reginald Elvis, M. Manoharan, J. Jayapal, and S. Kumaraguru, “Tailored Support Structures for Additive Manufacturing,” in *Advances in Additive Manufacturing and Joining*, ser. Lecture Notes on Multidisciplinary Industrial Engineering, Singapore: Springer, 2020, pp. 199–207, ISBN: 978-981-329-432-5. DOI: 10.1007/978-981-32-9433-2_17.
- [15] M. Zhou, Y. Liu, and Z. Lin, “Topology optimization of thermal conductive support structures for laser additive manufacturing,” *Computer Methods in Applied Mechanics and Engineering*, vol. 353, pp. 24–43, Aug. 15, 2019, ISSN: 0045-7825. DOI: 10.1016/j.cma.2019.03.054. Accessed: Feb. 20, 2025. [Online]. Available: <https://www.sciencedirect.com/science/article/pii/S0045782519301938>.
- [16] M. P. Bendsøe and O. Sigmund, *Topology Optimization*, 2nd ed. Springer Berlin, Heidelberg, Oct. 10, 2002, XIV, 370, ISBN: 978-3-540-42992-0.

- [17] J. Ye et al., “Topology optimisation of self-supporting structures based on the multi-directional additive manufacturing technique,” *Virtual and Physical Prototyping*, vol. 18, no. 1, e2271458, Dec. 31, 2023, ISSN: 1745-2759, 1745-2767. DOI: 10.1080/17452759.2023.2271458. Accessed: Feb. 20, 2025. [Online]. Available: <https://www.tandfonline.com/doi/full/10.1080/17452759.2023.2271458>.
- [18] M. Langelaar, “TOPOLOGY OPTIMIZATION FOR ADDITIVE MANUFACTURING WITH CONTROLLABLE SUPPORT STRUCTURE COSTS,” in *Proceedings of the VII European Congress on Computational Methods in Applied Sciences and Engineering (ECCOMAS Congress 2016)*, Crete Island, Greece: Institute of Structural Analysis and Antiseismic Research School of Civil Engineering National Technical University of Athens (NTUA) Greece, 2016, pp. 3689–3699, ISBN: 978-618-82844-0-1. DOI: 10.7712/100016.2065.5873. Accessed: Feb. 20, 2025. [Online]. Available: <http://www.eccomasprocedia.org/conferences/eccomas-congresses/eccomas-congress-2016/2065>.
- [19] G. Hornberger and P. Wiberg, “The Finite Element Method: An Introduction,” in *Numerical Methods in the Hydrological Sciences*, American Geophysical Union (AGU), 2005, pp. 1–10, ISBN: 978-1-118-70952-8. DOI: 10.1002/9781118709528.ch10. Accessed: Feb. 24, 2025. [Online]. Available: <https://onlinelibrary.wiley.com/doi/abs/10.1002/9781118709528.ch10>.
- [20] R. V. Kohn and G. Strang, “Optimal design and relaxation of variational problems, I,” *Communications on Pure and Applied Mathematics*, vol. 39, no. 1, pp. 113–137, Jan. 1986, ISSN: 0010-3640, 1097-0312. DOI: 10.1002/cpa.3160390107. Accessed: Feb. 24, 2025. [Online]. Available: <https://onlinelibrary.wiley.com/doi/10.1002/cpa.3160390107>.
- [21] K. Liu and A. Tovar, “An efficient 3D topology optimization code written in Matlab,” *Structural and Multidisciplinary Optimization*, vol. 50, no. 6, pp. 1175–1196, Dec. 2014, ISSN: 1615-147X, 1615-1488. DOI: 10.1007/s00158-014-1107-x.

- Accessed: Dec. 17, 2023. [Online]. Available: <http://link.springer.com/10.1007/s00158-014-1107-x>.
- [22] R. B. Haber, C. S. Jog, and M. P. Bendsøe, “A new approach to variable-topology shape design using a constraint on perimeter,” *Structural optimization*, vol. 11, no. 1, pp. 1–12, Feb. 1, 1996, ISSN: 1615-1488. DOI: 10.1007/BF01279647. Accessed: Sep. 12, 2024. [Online]. Available: <https://doi.org/10.1007/BF01279647>.
- [23] C. S. Jog, “Topology design of structures using a dual algorithm and a constraint on the perimeter,” *International Journal for Numerical Methods in Engineering*, vol. 54, no. 7, pp. 1007–1019, 2002, ISSN: 1097-0207. DOI: 10.1002/nme.457. Accessed: Feb. 24, 2025. [Online]. Available: <https://onlinelibrary.wiley.com/doi/abs/10.1002/nme.457>.
- [24] M. P. Bendsøe, *Optimization of Structural Topology, Shape, and Material*. Berlin, Heidelberg: Springer, 1995, ISBN: 978-3-662-03117-9 978-3-662-03115-5. DOI: 10.1007/978-3-662-03115-5. Accessed: Feb. 24, 2025. [Online]. Available: <http://link.springer.com/10.1007/978-3-662-03115-5>.
- [25] G. Allaire, *Shape Optimization by the Homogenization Method* (Applied Mathematical Sciences), S. S. Antman, J. E. Marsden, and L. Sirovich, red. New York, NY: Springer, 2002, vol. 146, ISBN: 978-1-4419-2942-6 978-1-4684-9286-6. DOI: 10.1007/978-1-4684-9286-6. Accessed: Feb. 24, 2025. [Online]. Available: <http://link.springer.com/10.1007/978-1-4684-9286-6>.
- [26] K. Suzuki and N. Kikuchi, “A homogenization method for shape and topology optimization,” *Computer Methods in Applied Mechanics and Engineering*, vol. 93, no. 3, pp. 291–318, Dec. 1, 1991, ISSN: 0045-7825. DOI: 10.1016/0045-7825(91)90245-2. Accessed: Feb. 24, 2025. [Online]. Available: <https://www.sciencedirect.com/science/article/pii/0045782591902452>.

- [27] M. Pietropaoli, F. Montomoli, and A. Gaymann, “Three-dimensional fluid topology optimization for heat transfer,” *Structural and Multidisciplinary Optimization*, vol. 59, no. 3, pp. 801–812, Mar. 1, 2019, ISSN: 1615-1488. DOI: 10.1007/s00158-018-2102-4. Accessed: Dec. 21, 2024. [Online]. Available: <https://doi.org/10.1007/s00158-018-2102-4>.
- [28] J. P. Groen and O. Sigmund, “Homogenization-based topology optimization for high-resolution manufacturable microstructures,” *International Journal for Numerical Methods in Engineering*, vol. 113, no. 8, pp. 1148–1163, Feb. 24, 2018, ISSN: 0029-5981, 1097-0207. DOI: 10.1002/nme.5575. Accessed: Feb. 24, 2025. [Online]. Available: <https://onlinelibrary.wiley.com/doi/10.1002/nme.5575>.
- [29] J. Alexandersen and B. S. Lazarov, “Topology optimisation of manufacturable microstructural details without length scale separation using a spectral coarse basis preconditioner,” *Computer Methods in Applied Mechanics and Engineering*, vol. 290, pp. 156–182, Jun. 15, 2015, ISSN: 0045-7825. DOI: 10.1016/j.cma.2015.02.028. Accessed: Feb. 24, 2025. [Online]. Available: <https://www.sciencedirect.com/science/article/pii/S0045782515000924>.
- [30] G. Allaire, P. Geoffroy-Donders, and O. Pantz, “Topology optimization of modulated and oriented periodic microstructures by the homogenization method,” *Computers & Mathematics with Applications, Simulation for Additive Manufacturing*, vol. 78, no. 7, pp. 2197–2229, Oct. 1, 2019, ISSN: 0898-1221. DOI: 10.1016/j.camwa.2018.08.007. Accessed: Feb. 24, 2025. [Online]. Available: <https://www.sciencedirect.com/science/article/pii/S0898122118304255>.
- [31] D. Kim, J. Lee, T. Nomura, E. M. Dede, J. Yoo, and S. Min, “Topology optimization of functionally graded anisotropic composite structures using homogenization design method,” *Computer Methods in Applied Mechanics and Engineering*, vol. 369, p. 113220, Sep. 1, 2020, ISSN: 0045-7825. DOI: 10.1016/j.

- cma.2020.113220. Accessed: Feb. 24, 2025. [Online]. Available: <https://www.sciencedirect.com/science/article/pii/S0045782520304059>.
- [32] J.-E. Kim, N.-K. Cho, and K. Park, “Computational homogenization of additively manufactured lightweight structures with multiscale topology optimization,” *Journal of Computational Design and Engineering*, vol. 9, no. 5, pp. 1602–1615, Sep. 8, 2022, ISSN: 2288-5048. DOI: 10.1093/jcde/qwac078. Accessed: Feb. 24, 2025. [Online]. Available: <https://academic.oup.com/jcde/article/9/5/1602/6660651>.
- [33] G. Allaire, F. Jouve, and H. Maillot, “Topology optimization for minimum stress design with the homogenization method,” *Structural and Multidisciplinary Optimization*, vol. 28, no. 2, pp. 87–98, Sep. 1, 2004, ISSN: 1615-1488. DOI: 10.1007/s00158-004-0442-8. Accessed: Feb. 24, 2025. [Online]. Available: <https://doi.org/10.1007/s00158-004-0442-8>.
- [34] G. Allaire, L. Cavallina, N. Miyake, T. Oka, and T. Yachimura, “The Homogenization Method for Topology Optimization of Structures: Old and New,” *Interdisciplinary Information Sciences*, vol. 25, no. 2, pp. 75–146, 2019. DOI: 10.4036/iis.2019.B.01.
- [35] M. P. Bendsøe, “Optimal shape design as a material distribution problem,” *Structural optimization*, vol. 1, no. 4, pp. 193–202, Dec. 1, 1989, ISSN: 1615-1488. DOI: 10.1007/BF01650949. Accessed: Feb. 24, 2025. [Online]. Available: <https://doi.org/10.1007/BF01650949>.
- [36] G. I. N. Rozvany, M. Zhou, and T. Birker, “Generalized shape optimization without homogenization,” *Structural optimization*, vol. 4, no. 3, pp. 250–252, Sep. 1, 1992, ISSN: 1615-1488. DOI: 10.1007/BF01742754. Accessed: Feb. 24, 2025. [Online]. Available: <https://doi.org/10.1007/BF01742754>.
- [37] “SIMP Method for Topology Optimization - 2019 - SOLIDWORKS Help,” Accessed: Feb. 24, 2025. [Online]. Available: https://help.solidworks.com/2019/english/SolidWorks/cworks/c_simp_method_topology.htm.

- [38] F. Wang, B. S. Lazarov, and O. Sigmund, “On projection methods, convergence and robust formulations in topology optimization,” *Structural and Multidisciplinary Optimization*, vol. 43, no. 6, pp. 767–784, Jun. 2011, ISSN: 1615-147X, 1615-1488. DOI: 10.1007/s00158-010-0602-y. Accessed: Feb. 25, 2025. [Online]. Available: <https://link.springer.com/10.1007/s00158-010-0602-y>.
- [39] B. S. Lazarov and O. Sigmund, “Filters in topology optimization based on Helmholtz-type differential equations,” *International Journal for Numerical Methods in Engineering*, vol. 86, no. 6, pp. 765–781, 2011, ISSN: 1097-0207. DOI: 10.1002/nme.3072. Accessed: Sep. 14, 2024. [Online]. Available: <https://onlinelibrary-wiley-com.proxyone.lib.nchu.edu.tw:8443/doi/abs/10.1002/nme.3072>.
- [40] A. B. Lambe and A. Czekanski, “Topology optimization using a continuous density field and adaptive mesh refinement,” *International Journal for Numerical Methods in Engineering*, vol. 113, no. 3, pp. 357–373, Jan. 20, 2018, ISSN: 0029-5981, 1097-0207. DOI: 10.1002/nme.5617. Accessed: Feb. 25, 2025. [Online]. Available: <https://onlinelibrary.wiley.com/doi/10.1002/nme.5617>.
- [41] “Performing Topology Optimization with the Density Method,” COMSOL, Accessed: Feb. 25, 2025. [Online]. Available: <https://www.comsol.com/blogs/performing-topology-optimization-with-the-density-method>.
- [42] S. Xu, Y. Cai, and G. Cheng, “Volume preserving nonlinear density filter based on heaviside functions,” *Structural and Multidisciplinary Optimization*, vol. 41, no. 4, pp. 495–505, 4 Apr. 1, 2010, ISSN: 1615-1488. DOI: 10.1007/s00158-009-0452-7. Accessed: Feb. 27, 2025. [Online]. Available: <https://link-springer-com.proxyone.lib.nchu.edu.tw:8443/article/10.1007/s00158-009-0452-7>.
- [43] M. P. Bendsøe and N. Kikuchi, “Generating optimal topologies in structural design using a homogenization method,” *Computer Methods in Applied Mechanics and Engineering*, vol. 71, no. 2, pp. 197–224, Nov. 1, 1988, ISSN: 0045-7825. DOI:

- 10.1016/0045-7825(88)90086-2. Accessed: Feb. 24, 2025. [Online]. Available: <https://www.sciencedirect.com/science/article/pii/0045782588900862>.
- [44] M. P. Bendsøe and O. Sigmund, “Material Interpolation Schemes in Topology Optimization,” *Archive of Applied Mechanics*, vol. 69, pp. 635–654, 1999, ISSN: 0939-1533.
- [45] T. Miki and T. Yamada, “Topology optimization considering the distortion in additive manufacturing,” *Finite Elements in Analysis and Design*, vol. 193, p. 103558, Oct. 2021, ISSN: 0168874X. DOI: 10.1016/j.finel.2021.103558. Accessed: May 28, 2024. [Online]. Available: <https://linkinghub.elsevier.com/retrieve/pii/S0168874X21000421>.
- [46] G. Misun et al., “Topology Optimization for additive manufacturing with distortion constraints,” *Computer Methods in Applied Mechanics and Engineering*, vol. 386, p. 114095, Dec. 1, 2021, ISSN: 0045-7825. DOI: 10.1016/j.cma.2021.114095. Accessed: Mar. 5, 2025. [Online]. Available: <https://www.sciencedirect.com/science/article/pii/S0045782521004266>.
- [47] L. Komini, M. Langelaar, and B. Kriegesmann, “Robust topology optimization considering part distortion and process variability in additive manufacturing,” *Advances in Engineering Software*, vol. 186, p. 103551, Dec. 2023, ISSN: 09659978. DOI: 10.1016/j.advengsoft.2023.103551. Accessed: Mar. 9, 2025. [Online]. Available: <https://linkinghub.elsevier.com/retrieve/pii/S0965997823001424>.
- [48] X. Guo, J. Zhou, W. Zhang, Z. Du, C. Liu, and Y. Liu, “Self-supporting structure design in additive manufacturing through explicit topology optimization,” *Computer Methods in Applied Mechanics and Engineering*, vol. 323, pp. 27–63, Aug. 15, 2017, ISSN: 0045-7825. DOI: 10.1016/j.cma.2017.05.003. Accessed: Mar. 5, 2025. [Online]. Available: <https://www.sciencedirect.com/science/article/pii/S004578251631564X>.

- [49] N. Zheng, X. Zhai, J. Jiang, and F. Chen, “Topology Optimization of Self-supporting Structures for Additive Manufacturing via Implicit B-spline Representations,” *Computer-Aided Design*, vol. 175, p. 103745, Oct. 1, 2024, ISSN: 0010-4485. DOI: 10.1016/j.cad.2024.103745. Accessed: Mar. 5, 2025. [Online]. Available: <https://www.sciencedirect.com/science/article/pii/S0010448524000721>.
- [50] W. Zhang and L. Zhou, “Topology optimization of self-supporting structures with polygon features for additive manufacturing,” *Computer Methods in Applied Mechanics and Engineering*, vol. 334, pp. 56–78, Jun. 1, 2018, ISSN: 0045-7825. DOI: 10.1016/j.cma.2018.01.037. Accessed: Mar. 5, 2025. [Online]. Available: <https://www.sciencedirect.com/science/article/pii/S0045782518300392>.
- [51] W. Ameen, A. Al-Ahmari, and M. K. Mohammed, “Self-supporting overhang structures produced by additive manufacturing through electron beam melting,” *The International Journal of Advanced Manufacturing Technology*, vol. 104, no. 5, pp. 2215–2232, 5 Oct. 1, 2019, ISSN: 1433-3015. DOI: 10.1007/s00170-019-04007-3. Accessed: Mar. 5, 2025. [Online]. Available: <https://link-springer-com.proxyone.lib.nchu.edu.tw:8443/article/10.1007/s00170-019-04007-3>.
- [52] S. Xu, J. Liu, Y. Sun, X. Li, and Y. Ma, “Support structure topology optimization considering the residual distortion for laser powder bed fusion metal additive manufacturing,” *Structural and Multidisciplinary Optimization*, vol. 67, no. 10, pp. 1–20, 10 Oct. 1, 2024, ISSN: 1615-1488. DOI: 10.1007/s00158-024-03883-y. Accessed: Mar. 5, 2025. [Online]. Available: <https://link-springer-com.proxyone.lib.nchu.edu.tw:8443/article/10.1007/s00158-024-03883-y>.
- [53] T.-U. Lee and Y. M. Xie, “Simultaneously optimizing supports and topology in structural design,” *Finite Elements in Analysis and Design*, vol. 197, p. 103633, Dec. 1, 2021, ISSN: 0168-874X. DOI: 10.1016/j.finel.2021.103633. Accessed:

- Feb. 20, 2025. [Online]. Available: <https://www.sciencedirect.com/science/article/pii/S0168874X21001177>.
- [54] D. J. Lohan, E. M. Dede, and J. T. Allison, “A study on practical objectives and constraints for heat conduction topology optimization,” *Structural and Multidisciplinary Optimization*, vol. 61, no. 2, pp. 475–489, 2 Feb. 1, 2020, ISSN: 1615-1488. DOI: 10.1007/s00158-019-02369-6. Accessed: Mar. 4, 2025. [Online]. Available: <https://link-springer-com.proxyone.lib.nchu.edu.tw:8443/article/10.1007/s00158-019-02369-6>.
- [55] D. J. Lohan, E. M. Dede, and J. T. Allison, “Topology optimization for heat conduction using generative design algorithms,” *Structural and Multidisciplinary Optimization*, vol. 55, no. 3, pp. 1063–1077, Mar. 1, 2017, ISSN: 1615-1488. DOI: 10.1007/s00158-016-1563-6. Accessed: Feb. 5, 2024. [Online]. Available: <https://doi.org/10.1007/s00158-016-1563-6>.
- [56] A. Iga, S. Nishiwaki, K. Izui, and M. Yoshimura, “Topology optimization for thermal conductors considering design-dependent effects, including heat conduction and convection,” *International Journal of Heat and Mass Transfer*, vol. 52, no. 11, pp. 2721–2732, May 1, 2009, ISSN: 0017-9310. DOI: 10.1016/j.ijheatmasstransfer.2008.12.013. Accessed: Sep. 4, 2024. [Online]. Available: <https://www.sciencedirect.com/science/article/pii/S0017931009000271>.
- [57] R. Huang, N. Dai, X. Cheng, and L. Wang, “Topology optimization of lattice support structures for heat conduction in selective laser melting,” *The International Journal of Advanced Manufacturing Technology*, vol. 109, no. 7–8, pp. 1841–1851, Aug. 2020, ISSN: 0268-3768, 1433-3015. DOI: 10.1007/s00170-020-05741-9. Accessed: Feb. 24, 2024. [Online]. Available: <https://link.springer.com/10.1007/s00170-020-05741-9>.
- [58] S. Ogawa and T. Yamada, “Topology optimization for transient response problems involving thermoelastic materials,” *Finite Elements in Analysis and Design*, vol. 201, p. 103695, Apr. 1, 2022, ISSN: 0168-874X. DOI: 10.1016/j.

- [finel.2021.103695](https://www.sciencedirect.com/science/article/pii/S0168874X21001694). Accessed: May 23, 2024. [Online]. Available: <https://www.sciencedirect.com/science/article/pii/S0168874X21001694>.
- [59] *FreeCAD*, FreeCAD Team. [Online]. Available: <https://www.freecad.org/>.
- [60] S. Leopold, “Minimally Invasive Total Knee Arthroplasty for Osteoarthritis,” *The New England journal of medicine*, vol. 360, pp. 1749–58, May 1, 2009. DOI: 10.1056/NEJMct0806027.
- [61] G. Lee, Y. Joo, and S. J. Kim, “On the Objective Function for Topology Optimization of Heat Sinks,” *IEEE Transactions on Components, Packaging and Manufacturing Technology*, vol. 11, no. 11, pp. 1776–1782, Nov. 2021, ISSN: 2156-3985. DOI: 10.1109/TCPMT.2021.3120383. Accessed: Mar. 17, 2025. [Online]. Available: <https://ieeexplore.ieee.org/document/9576508>.
- [62] G. H. Yoon, “Topological design of heat dissipating structure with forced convective heat transfer,” *Journal of Mechanical Science and Technology*, vol. 24, no. 6, pp. 1225–1233, 6 Jun. 1, 2010, ISSN: 1976-3824. DOI: 10.1007/s12206-010-0328-1. Accessed: Mar. 17, 2025. [Online]. Available: <https://link.springer-com.proxyone.lib.nchu.edu.tw:8443/article/10.1007/s12206-010-0328-1>.
- [63] T. E. Bruns, “Topology optimization of convection-dominated, steady-state heat transfer problems,” *International Journal of Heat and Mass Transfer*, vol. 50, no. 15, pp. 2859–2873, Jul. 1, 2007, ISSN: 0017-9310. DOI: 10.1016/j.ijheatmasstransfer.2007.01.039. Accessed: Mar. 17, 2025. [Online]. Available: <https://www.sciencedirect.com/science/article/pii/S0017931007001330>.
- [64] R. Davis et al., “A comprehensive review on metallic implant biomaterials and their subtractive manufacturing,” *The International Journal of Advanced Manufacturing Technology*, vol. 120, no. 3–4, pp. 1473–1530, 2022, ISSN: 0268-3768. DOI: 10.1007/s00170-022-08770-8. pmid: 35228769. Accessed: Mar. 17, 2025. [Online]. Available: <https://www.ncbi.nlm.nih.gov/pmc/articles/PMC8865884/>.

- [65] K. Svanberg, “The method of moving asymptotes—a new method for structural optimization,” *International Journal for Numerical Methods in Engineering*, vol. 24, no. 2, pp. 359–373, 1987, ISSN: 1097-0207. DOI: 10.1002/nme.1620240207. Accessed: Mar. 18, 2025. [Online]. Available: <https://onlinelibrary.wiley.com/doi/abs/10.1002/nme.1620240207>.
- [66] *nTop*, nTopology Inc. [Online]. Available: <https://www.ntop.com/>.
- [67] Hexagon AB, *Process Properties Infosheet*.
- [68] P.-H. Chung, J.-R. Zhuang, and C.-H. Pan, “Evaluation and prediction of thermal defects in SLM-manufactured tibial components using FEM-based deep learning and statistic methods,” *The International Journal of Advanced Manufacturing Technology*, vol. 134, no. 1, pp. 691–709, Sep. 1, 2024, ISSN: 1433-3015. DOI: 10.1007/s00170-024-14139-w. Accessed: Mar. 18, 2025. [Online]. Available: <https://doi.org/10.1007/s00170-024-14139-w>.
- [69] H. T. Chowdhury, T. N. Palleda, N. Kakuta, and K. Kakehi, “Effects of Pre-heating on Thermal Behavior in Inconel 718 Processed by Additive Manufacturing,” *Thermo*, vol. 4, no. 1, pp. 48–64, 1 Mar. 2024, ISSN: 2673-7264. DOI: 10.3390/thermo4010005. Accessed: Mar. 18, 2025. [Online]. Available: <https://www.mdpi.com/2673-7264/4/1/5>.